POLITECNICO
MILANO 1863

SCUOLA DI INGEGNERIA INDUSTRIALE
E DELL'INFORMAZIONE

Transfer trajectory and operational orbit selection for Earth-Moon L_2 near rectilinear halo orbits through invariant manifolds

Tesi di Laurea Magistrale in
Space Engineering - Ingegneria Spaziale

Author: **Enis Arıkan**

Student ID: 10775709
Advisor: Prof. Camilla Colombo
Co-advisors: Dr. Elisa Maria Alessi
Academic Year: 2021-22

Copyright© April 2023 by Enis Arıkan.

All rights reserved.

This content is original, written by the Author, Enis Arıkan. All the non-originals information, taken from previous works, are specified and recorded in the Bibliography.

When referring to this work, full bibliographic details must be given, i.e.

Arıkan Enis, "Transfer trajectory and operational orbit selection for Earth-Moon L_2 near rectilinear halo orbits through invariant manifolds". 2023, Politecnico di Milano, Master Thesis in Space Engineering, Supervisor: Camilla Colombo, Co-supervisor: Elisa Maria Alessi.

Abstract

The aim of this thesis is to conduct a parametric analysis of transfer trajectory options to the Earth-Moon L_2 Near-Rectilinear Halo Orbit (NRHO) family by utilising invariant manifolds. Due to their high stability characteristics, the NRHO family is the target of many present and future space applications including the NASA Gateway [9]. In this study, the generation and identification of these orbits are discussed along with a detailed eclipse analysis. The transfer design to the operational orbit utilises the homoclinic connections along the L_2 point by using an intermediate Halo orbit. A parametric study is conducted to see the maneuver cost variation for different Halo and NRHO pairs. As a preliminary analysis, the transfer to the intermediate halo trajectory is conducted by merging a two-body solution with the invariant manifolds proper of the Circular Restricted Three-Body Problem (CRTBP). As a parking orbit, Low Earth Orbits (LEO) and Geostationary Transfer Orbits (GTO) are studied with varying perigee radii. Additionally, an alternative insertion point on the Halo stable manifold is studied. Then the most feasible option is refined by applying a CRTBP model. Both segments, parking orbit to halo and halo to NRHO, are merged and a trade-off is conducted based on the cost, transfer time and eclipse characteristics. The resulting transfer trajectories are proposed as a backup option for the REMEC mission [1].

Keywords: invariant manifolds, periodic orbits, transfer design, Lagrange points, NRHO, Earth-Moon system, parametric analysis

Abstract in lingua italiana

Lo scopo di questa tesi è fornire un'analisi parametrica dei possibili trasferimenti da un'orbita di parcheggio intorno alla Terra a un'orbita del tipo "Near Rectilinear Halo Orbit" (NRHO) intorno al punto di librazione L_2 nel sistema Terra-Luna attraverso le varietà invarianti iperboliche. molteplice. Grazie alla loro stabilità, la famiglia di orbite NRHO è obiettivo di molte missioni spaziali, inclusa la stazione lunare prevista dalla NASA [9]. In questo studio, il calcolo e l'analisi di queste orbite sono presentati in maniera dettagliata, includendo anche lo studio delle possibili eclissi. Il trasferimento all'orbita operativa utilisza le connessioni omocliniche associate al punto L_2 utiliszando un'orbita Halo intermedia. Viene condotto uno studio parametrico per vedere la variazione del costo della manovra per diverse combinazioni Halo e NRHO. Come analisi preliminare il trasferimento all'orbita Halo intermedia si ottiene unendo una soluzione a due corpi con le varietà invarianti del Problema Ristretto Circolare dei Tre Corpi (CRTBP). Come orbita parcheggio, l'orbita terrestre bassa (LEO) e orbita di trasferimento geostazionaria (GTO) sono studiate assumendo diversi valori di perigeo. Inoltre, un inserimento alternativo viene studiato in base al punto di inserimento sulla varietà stabile di halo. Quindi l'opzione migliore viene perfezionata applicando un modello CRTBP. Entrambi i segmenti vengono uniti e le conclusioni sul trasferimento più conveniente vengono tratte in base al costo, al tempo di trasferimento e alla durata delle eclissi. Le risultanti traiettorie di trasferimento sono proposte come opzione di backup per la missione REMEC [1].

Parole chiave: varietà invarianti, orbite periodiche, disegno di trasferimento, punti di Lagrange, NRHO, Terra-Luna sistema, analisi parametrica

Contents

Abstract **iii**

Abstract in lingua italiana **v**

Contents **vii**

1 Introduction **1**

1.1 Literature review: past and future missions to Earth-Moon L_2, L_4 and L_5 . 2

1.2 Literature review: transfer trajectory design to Earth-Moon L_2 3

1.3 Current work 5

2 Background: Mathematical Models **7**

2.1 Circular restricted three-body problem 7

2.1.1 Rotating and inertial frames 8

2.1.2 Equations of motion 12

2.1.3 Pseudo-potential function 13

2.1.4 Lagrange points 15

2.2 Basic numerical methods 16

2.2.1 Poincaré map 17

2.2.2 State transition matrix 18

2.2.3 Differential corrector 20

3 Operational Orbit Design in Earth-Moon L_2 **23**

3.1 Generating Periodic Halo Orbits 23

3.2 Halo and NRHO families 25

3.3 Eclipse analysis for EM-L2 NRHO family 30

3.3.1 The definitions of shadow regions 31

3.3.2 Eclipse analysis results 33

4 Parking Orbit to Halo Transfer Trajectory Design **39**

4.1 Computing manifolds 39
4.2 Earth parking orbit design 42
4.2.1 LEO to GTO transfer 42
4.3 Parking orbit to manifold insertion 43
4.3.1 Hohmann maneuver approach 43
4.3.2 Targeting and optimizing in CRTBP 52

5 Halo to NRHO Transfer Design 57
5.1 Sphere of influence 57
5.2 Defining bounding sphere 58
5.3 Searching for optimal connection points 59
5.3.1 Defining two-body parameters 59
5.3.2 Selection of manifold pair 60
5.3.3 Selection of connection states 61
5.4 Transfer design between two manifolds 61

6 Operational Orbit Selection and Complete Trajectory Design 65

7 Summary and future developments 75

Bibliography 77

List of Figures 81

List of Tables 83

List of Symbols 85

Acknowledgements 87

1 Introduction

The dynamical behaviour of two celestial objects under their mutual gravitational attraction is well understood by the two-body Problem (TBP). This dynamical model could be used to patch the trajectory of the spacecraft in a multi-body environment by connecting conic sections whenever the spacecraft enters the sphere of influence of a given celestial body. As a practical example, this method has been implemented for the preliminary trajectory design of the Apollo and Voyager missions. A different approach to this problem involves the implementation of hyperbolic manifold dynamics which is natural dynamics given by the simultaneous and comparable gravitational attraction of two massive bodies on a small body to conduct transfer, station keeping, and end-of-life maneuvers. Furthermore, this dynamical model could be used to reduce the Δv compared to the traditional methods by reducing the mission cost significantly such as in the case of the Genesis mission, where a Δv of 100 m/s was saved [5].

Let us consider two massive bodies and one with a mass much lower than the other two. This is a simplification of the general Three-Body Problem (3BP), called Restricted Three-Body Problem (RTBP), that applies to many situations in the solar system. If the two primaries follow a circular orbit around their center of mass, we can further simplify the equations of motion. This is the so-called Circular Restricted Three-Body Problem (CRTBP). In 1772 Lagrange proved that five equilibrium points exist in the CRTBP model synodic frame [28]; three on the axis connecting the two bodies and two at an equilateral distance. At these points, the forces acting on the satellite compensate each other such that the relative position to the primaries remains constant in the rotating frame. Since their discovery, the Lagrangian points in any three-body system have been a great subject of interest for the science and engineering community. A properly placed spacecraft in this region shall follow an orbit with periodic or quasi-periodic behaviour. Moreover, as explained for instance in [22], a periodic orbit around L_2 could be an optimal position to observe the deep space while an orbit around L_1 is best suited for Sun observation. The trajectory design in this thesis is based on the Radiation Environment Monitor for Energetic Cosmic rays (REMEC) mission. REMEC is a CubeSat mission proposed by European Space Agency (ESA) aimed to monitor deep space for cosmic rays. The backup

operational orbit for the mission is selected as a NRHO at Earth-Moon L_2. Due to this, right now Earth-Moon L_2 is the main target under the study.

In the late 1960s, Farquhar studied the analytical approximations for the three-dimensional periodic orbit at the Earth-Moon system [10]. There, he defined the halo orbits as three-dimensional periodic orbits in the vicinity of the collinear equilibrium points. Near-Rectilinear Halo Orbits (NRHOs) are a subset of these halo trajectories. They differ from halos by having a more stable nature, thus allowing a low-cost station-keeping design. To generate these trajectories in the CRTBP, a general algorithm is given in [15]. Furthermore, the works in [31], [17], [32], and [4] proposed a transfer design based on impulsive maneuvers, while [25] proposed low-thrust missions. Additionally, station-keeping designs for periodic orbits around libration points in the Earth-Moon system have been conducted in [33], [24], and [11].

1.1. Literature review: past and future missions to Earth-Moon L_2, L_4 and L_5

Based on the requirements for the REMEC, in table 1.1, previous and future missions to Earth-Sun Lagrange points L_4, L_5, and L_2 are presented. L_4 and L_5 included since possible rideshare launcher transfer could be utilised to those locations. Currently, 16 missions have been sent to the Sun-Earth Lagrangian points and future missions such as PLATO (ESA), LiteBIRD (JAXA), and ARIEL (ESA) are in development. Regarding previous missions, Herschel, Planck, and Gaia are the most suitable candidates to obtain a preliminary idea about the space environment experienced and the mission design applied in the L_2 point. In her work, Soldini [26], studied the behaviour of these spacecraft under the effect of solar radiation perturbation in the ER3BP. Five equilibrium points still exist in the ER3BP, however, now the rotating frame has a non-uniform angular velocity.

The REMEC mission is designated as a CubeSat. Although past missions provide invaluable insight into the expected trajectory, they are massive compared to a CubeSat. Regarding the CubeSats, most of the state of art comes from academic studies. One such mission is a study conducted by Viscio [30] which proposes a preliminary design of a 6U CubeSat for Earth-Sun points for space-weather evaluations.

Satellite Name	Launch Date	Target Point	Mission Status	Operator	Launch Mass [kg]	Duration [years]
Comet Interceptor	2029	SE L_2	In progress	ESA/JAXA	850	5
ARIEL	2029	SE L_2	In progress	ESA	1300	4
LiteBIRD	2028	SE L_2	In progress	JAXA/ISAS	450	3
PLATO	2026	SE L_2	In progress	ESA	2134	4
WFIRST	2027	SE L_2	In progress	NASA/GSFC	4166	5
Euclid	2023	SE L_2	In progress	ESA	2160	6
JWST	2021	SE L_2	Active	NASA/ESA/CSA	6161	10
Spektr-RG	2019	SE L_2	Active	Roscosmos/DLR	2712	6.5
Gaia	2013	SE L_2	Retired	ESA	2029	8
Chang'e 2	2010	SE L_2	Retired	CNSA	2480	4
Planck	2009	SE L_2	Retired	ESA	1950	4
Herschel	2009	SE L_2	Retired	ESA	3400	4
Wind	1994	SE L_2	Active	NASA	1250	27
WMAP	2001	SE L_2	Retired	NASA	835	9
OSIRIS-Rex	2016	SE L_4	Active	NASA	2110	7
STEREO-A	2006	SE L_4	Active	NASA	619	15
ESA Vigil	2020	SE L_5	In progress	ESA	-	-
Hayabusa 2	2014	SE L_5	Active	JAXA	610	7
STEREO-B	2006	SE L_5	Lost Contact	NASA	619	9
SST	2003	SE L_5	Retired	NASA	950	17

Table 1.1: Missions related to Earth-Sun Lagrange points L_4, L_5 and L_2

1.2. Literature review: transfer trajectory design to Earth-Moon L_2

A literature review for the transfers from the Earth to Earth-Moon L2 NRHO has been conducted and presented in Table 1.2. Target orbit parameters, i.e., perilune, apolune and period, and resonance are presented. The period here is defined as the one full rotation around the Moon while the resonance is the ratio of the Moon's period around Earth to the orbital period of the spacecraft around the Moon. Hitherto, seven possible transfer

methods have been studied to reach NRHO from the literature.

Parking Orbit	Target Point				Δv [m/s]	TOF [years]	Transfer Type
	Perilune [km]	Apolune [km]	Resonance	Period [days]			
Circular LEO	3250	71000	9:2	6.5	398.0	-	A
Circular LEO	5750	75000	4:1	7.3	393.0	-	A
Circular LEO	2000	68000	-	5.9	404.0	-	A
Circular LEO	3250	71000	9:2	6.5	6.3	136	B
Circular LEO	5750	75000	4:1	7.3	26.0	104	B
sGTO	3269	-	9:2	6.573	2749.5	29.02	C
sGTO	2047	-	24:5	6.074	2743.0	28.96	C
sGTO	5542	-	4:1	7.322	2760.1	29.12	C
sGTO	3269	-	9:2	6.573	1936.5	78.72	D
sGTO	2047	-	24:5	6.074	1880.6	77.85	D
sGTO	5542	-	4:1	7.322	2174.1	82.25	D
sGTO	3269	-	9:2	6.573	1540.8	93.19	E
sGTO	2047	-	24:5	6.074	1506.4	92.89	E
sGTO	5542	-	4:1	7.322	1720.7	9.334	E
Circular LEO	4000	-	-	7.0	456.0	5.1	A
Circular LEO	7000	-	-	7.7	3683.0	>54.6	F
Circular LEO	7000	-	-	7.7	3677.0	>54.6	F
Circular LEO	7000	-	-	7.7	3740.0	>47.9	F
Circular LEO	7000	-	-	7.7	3800.0	>45.4	F
Circular LEO	7000	-	-	7.7	3850.0	>43.6	F
Circular LEO	7000	-	-	7.7	3904.0	>43.0	F
Circular LEO	5000	-	4:1	7.322	3953.0	-	G

Table 1.2: Transfer options from Earth to EM L2 NRHO.

Transfer type A has been studied in [31] and [17]. An impulsive maneuver injects the spacecraft into a Moon flyby trajectory. Then a powered gravity assist targets the desired NRHO. Finally, the last burn inserts the satellite into a nominal NRHO. As stated in [31] and [17], the insertion plus powered flyby cost for this type of transfer lies in the range of 400 – 450 m/s for the low perilune NRHOs. Importantly, no data was provided in the literature regarding the initial burn to place the satellite into the flyby trajectory from

the parking orbit. For our analysis, as stated in [32], we can consider that a 3.15 km/s maneuver would be sufficient to place the satellite into the translunar trajectory. Like A, type B transfers utilise an impulsive burn to place the spacecraft on a ballistic lunar capture trajectory and a final burn to insert the spacecraft into its final operational orbit. According to a study presented in [31], insertion costs could be reduced vastly for this type of transfer, dropping to merely 6.3 m/s. Here also no data was provided for the initial burn to leave the parking orbit. Low-thrust options have been taken into consideration as well. According to the work presented in [25], three types of transfer have been proposed. Parking orbit is sGTO with orbital parameters presented in Table 5-8. Type C transfer targets a time-optimal solution while targeting the NRHO directly, requiring a Δv of at least 2743.0 m/s. Like type C, type D aims to achieve a time-optimal trajectory however now utilising the manifolds of the Earth-Moon space system. As a result, the Δv reduces down to 1880.6 m/s at the expense of time of flight which increases drastically compared to the former case. Finally, the last type E targets a fuel-optimal trajectory, in which the Δv cost is down to 1506.4 m/s, while the time of flight increases slightly to 92.894 days.

Type F has been studied in [16]. Only impulsive maneuvers were applied. Starting from a 200x200 km LEO, the spacecraft was placed on an L2 halo orbit and then inserted into a NRHO by utilising manifold dynamics. Different intermediate halo orbits for the same target have been presented in Table 1.2, where the lowest Δv is 3.677 m/s. As studied in [34], type G is the most direct approach. Again, only impulsive maneuvers were applied. Starting from a 200x200 km LEO, the spacecraft was placed on a NRHO directly, resulting in a Δv of 3953 m/s.

In conclusion, if we consider as target a NRHO in the Earth-Moon system, according to the literature, the cost to transfer from a GTO would be between 1.2 - 1.7 km/s, while from LEO at least 2 km/s higher. The highest cost is associated with the departure from the Earth's neighborhood, about 1 km/s from a GTO and 3 km/s from a LEO. The second maneuver needed to reach an L2 Earth-Moon NRHO can be optimized and studied in various ways. The most optimistic scenario is 200 m/s, but likely it is a bit higher.

1.3. Current work

This thesis aims to conduct a parametric study for the transfers targeting NRHOs at the $EM - L_2$ by utilising the invariant manifolds. The major contributions are presented in Chapter 4, 5 and 6. Chapter 4 focuses on the trajectory design to the halo family at $EM - L_2$ from an Earth parking orbit. Multiple options for parking orbit and manifold insertion points are studied by utilising two-body and three-body dynamics. In Chapter

5, homoclinic connections are implemented between halo family and NRHO subset for multiple combinations showing the behaviour of the transfer cost with respect to periodic orbit couple selections. Chapter 6 presents the complete trajectory design in CRTBP for multiple operational and intermediate halo orbit selections.

The thesis is organized as follows: in Chapter 2 the mathematical background regarding the methodology is explained in detail along with the terminology. In Chapter 3 the halo family around $EM-L_2$ is generated and the NRHO subset is characterized along with an eclipse analysis. In Chapter 4 a parametric analysis is conducted for the transfer between an Earth parking orbit and $EM-L_2$ halo with various parking and halo orbit options, and insertion geometries. The behaviour of the LEO and GTO parking orbits with varying perigees are analyzed by combining two-body and three-body dynamics. Additionally, two different manifold insertion point selections are compared. The optimum selections here are refined by implementing complete CRTBP dynamics. Chapter 5 focuses on the parametric analysis of the transfer between a halo and a NRHO by utilising homoclinic connections. In Chapter 6, the results from the previous two chapters are merged to obtain the complete transfer trajectory and a trade-off is done to obtain the best options. Finally in Chapter 7, the conclusions, summary and the future work to be done are explained.

2 Background: Mathematical Models

In this chapter, the methods and mathematical models implemented in this study shall be explained in detail.

2.1. Circular restricted three-body problem

In its simplest form, the motion of a spacecraft in space could be described by the two-body problem. In this model, a further simplification can be introduced if the mass of one object is very small compared to the other such as a satellite orbiting a planet. Then the two-body problem can be defined as,

$$\ddot{\bar{R}} = -\frac{Gm}{|\bar{R}|^3}\bar{R}, \tag{2.1}$$

Here the vector $\bar{R}$ represents the position vector of the spacecraft with respect to the center of the massive body, m is the mass of the planet and G is the gravitational constant in the inertial frame. This model could be augmented in such a way that the effect of n number of massive bodies is taken into account. In a three-body scenario, the model can be expressed as,

$$\ddot{\bar{R}}_3 = -\frac{Gm_1}{|\bar{R}_{13}|^3}\bar{R}_{13} - \frac{Gm_2}{|\bar{R}_{23}|^3}\bar{R}_{23}, \tag{2.2}$$

This is defined as the restricted three-body problem. Here the "restricted" term is due to the assumption that the third mass in the system is assumed to be small compared to the other two. A further simplification is to assume that the primaries in the system follow a circular orbit around their common center of mass hence resulting in the circular restricted three-body problem. As stated before, in this thesis the motion of the spacecraft in the Earth-Moon system is analyzed using this dynamics model. No additional perturbations

are taken into account.

2.1.1. Rotating and inertial frames

Two sets of coordinate frames are required to explain and define the circular restricted three-body problem: the inertial and the rotating reference systems. The inertial frame is assumed to be a non-rotating and non-accelerating frame with respect to distant stars. In this study, the inertial reference frame elements shall be presented with $[\hat{X}\ \hat{Y}\ \hat{Z}]$.

The rotating frame as the name suggests together with the primary with the smallest mass with respect to the bigger one. The x-axis of the rotating frame is along the apse line connecting the two primaries and the frame rotates around its z-axis. In this study, the rotating reference frame elements shall be presented with $[\hat{x}\ \hat{y}\ \hat{z}]$.

The geometry of the frames is represented in Figure 2.1. The origin of the two frames is assumed to be at the barycenter of the primaries with the z-axis coinciding with each other. At $t = 0$ all three axes are aligned with each other.

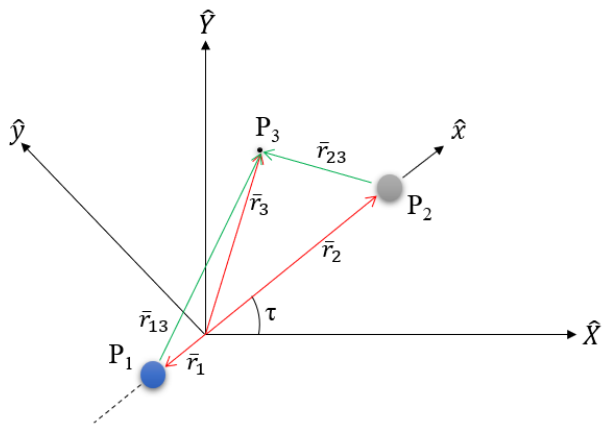

Figure 2.1: Rotating and inertial frames

Non-dimensionalization of states

To have a better grasp of the reference frame transformations in this study, it is necessary to explain the concept of non-dimensionalization. The states in the rotating frames are generally represented in non-dimensional values whereas in inertial frames classical dimensions are utilised. Non-dimensionalization is a useful step to derive the generalized versions of the differential equations. Three characteristic dimensions, length, time, and mass, are selected to apply the method. The distance between two primaries is selected as the characteristic length. Hence the non-dimensional distance between the two celestial

bodies becomes 1. For the characteristic mass, the total mass of the primaries is chosen as,

$$m_n = m_1 + m_2 \tag{2.3}$$

Here we can introduce the mass parameter for the system as,

$$\mu = \frac{m_2}{m_n} \tag{2.4}$$

Hence the mass of the first primary represented as,

$$1 - \mu = \frac{m_1}{m_n} \tag{2.5}$$

Hence the non-dimensional total mass of the system becomes equal to 1. Here it is observed that the resulting mass representations define the position of the primaries in the rotating reference frame such that the vectors defined as,

$$\begin{cases} \bar{r}_1 = -\mu\hat{x}, \\ \bar{r}_2 = (1-\mu)\hat{x}, \end{cases} \tag{2.6}$$

Finally, the characteristic time is defined as,

$$t_c = \sqrt{\frac{l_c^3}{\mu_1 + \mu_2}}, \tag{2.7}$$

Here μ_1 and μ_2 are the standard gravitational parameters of the primaries and l_c is the characteristic length. The resulting non-dimensional time demonstrates that, namely, a circular orbit around the barycenter, the system has a non-dimensional mean motion equal to 1 demonstrated as,

$$n = \sqrt{\frac{\mu_1 + \mu_2}{l_c^3}}, \tag{2.8}$$

As a result, the angle of rotation between the two frames is,

$$\tau = \frac{t}{t_n}, \tag{2.9}$$

In the Earth-Moon system, the resulting non-dimensionalizing parameters are defined in Table 2.1,

l_c	t_c	μ
$[km]$	$[s]$	$[-]$
384400	375189.5	0.0121505856

Table 2.1: Non-dimesionalizing parameters for Earth-Moon system.

Rotating to inertial frame transformation

To explain the R3BP dynamics, it is necessary to have a clear explanation of the transformation between the rotating frame and the inertial frame. The problem geometry is presented in Figure 2.1. As stated before, at t_0, both the frames are assumed to be coinciding and the rotation occurs around the z-axis, so only a rotation around that axis is sufficient to align the frames. Additionally, in order to convert from non-dimensional units, multiplication with l_n is required. Equation (2.10) represents the transformation,

$$\begin{pmatrix} X \\ Y \\ Z \end{pmatrix} = l_n A_t \begin{pmatrix} x \\ y \\ z \end{pmatrix} \tag{2.10}$$

Here, the states $[x\ y\ z]$ and $[X\ Y\ Z]$ are the positions with respect to the origin of the frames. So in order to obtain the inertial state with respect to the Earth, $[x\ y\ z]$ needs to define the distance to Earth in the rotating frame. Additionally, the transformation matrix is defined as,

$$A_t = \begin{bmatrix} cos(\tau) & -sin(\tau) & 0 \\ sin(\tau) & cos(\tau) & 0 \\ 0 & 0 & 1 \end{bmatrix}, \tag{2.11}$$

To achieve the conversion of velocity components, the derivative of Equation (2.10) reads,

$$\begin{pmatrix} \dot{X} \\ \dot{Y} \\ \dot{Z} \end{pmatrix} = l_n \dot{A}_t \begin{pmatrix} x \\ y \\ z \end{pmatrix} + l_n A_t \begin{pmatrix} \dot{x} \\ \dot{y} \\ \dot{z} \end{pmatrix} \tag{2.12}$$

Here, the derivative of the transformation matrix is defined as,

$$\dot{A}_t = \begin{bmatrix} -sin(\tau) & -cos(\tau) & 0 \\ cos(\tau) & -sin(\tau) & 0 \\ 0 & 0 & 0 \end{bmatrix}, \tag{2.13}$$

Finally, we obtain,

$$\begin{pmatrix} \dot{X} \\ \dot{Y} \\ \dot{Z} \end{pmatrix} = l_n A_t \begin{pmatrix} \dot{x} - y \\ \dot{y} + x \\ \dot{z} \end{pmatrix} \tag{2.14}$$

As a final step, a division with non-dimensional time is required to obtain the correct dimensional velocity.

Inertial Frame to Rotating Frame Transformation

For the inertial frame to the rotating frame, the algorithm is reversed. Now starting from the inertial frame coordinates, the position in non-dimensional units is obtained from (2.15).

$$\begin{pmatrix} x \\ y \\ z \end{pmatrix} = \frac{1}{l_n} A_t^{-1} \begin{pmatrix} X \\ Y \\ Z \end{pmatrix} \tag{2.15}$$

and to achieve the conversion of velocity components, Equation (2.16) is used. Again here the derivatives need to be corrected by multiplying by non-dimensional time t_n,

$$\begin{pmatrix} \dot{x} \\ \dot{y} \\ \dot{z} \end{pmatrix} = \frac{1}{l_n} A_t^{-1} \begin{pmatrix} \dot{X} + y \\ \dot{Y} - x \\ \dot{Z} \end{pmatrix} \tag{2.16}$$

To provide an example, in Figure 2.2, the representations of a NRHO are presented in the rotating and inertial frames. It is clearly seen that the motion in the rotating frame is much simpler to visualize and observe the behaviour of the periodic orbit.

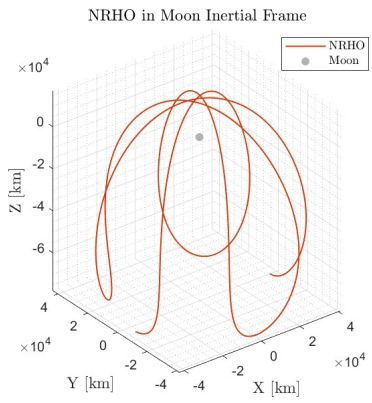

(a) Moon inertial frame.

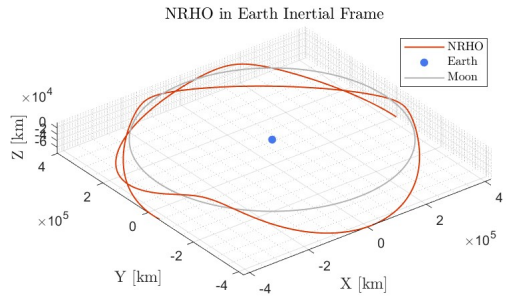

(b) Earth inertial frame.

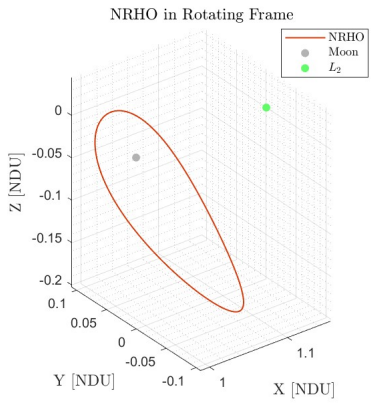

(c) Rotating frame.

Figure 2.2: Representation of NRHO in various frames.

2.1.2. Equations of motion

As explained before non-dimensionalization is a useful step to represent the problem involving the three-body problem. As a result, Equation (2.2) can be written as,

$$\ddot{\bar{r}}_3 = -\frac{1-\mu}{|\bar{r}_{13}|^3}\bar{r}_{13} - \frac{\mu}{|\bar{r}_{23}|^3}\bar{r}_{23}, \tag{2.17}$$

Now, let's define the position vector of the satellite in the rotating frame in non-dimensional coordinates,

$$\bar{r}_3 = x\hat{x} + y\hat{y} + z\hat{z}, \tag{2.18}$$

So the relative position of the spacecraft with respect to the primaries is,

$$\begin{cases} \bar{r}_{13} = (x+\mu)\hat{x} + y\hat{y} + z\hat{z}, \\ \bar{r}_{23} = (x+\mu-1)\hat{x} + y\hat{y} + z\hat{z}, \end{cases} \tag{2.19}$$

Taking the derivative once, the expression for the velocity vector is,

$$\dot{\bar{r}}_3 = (\dot{x} - y)\hat{x} + (\dot{y} + x)\hat{y} + \dot{z}\hat{z}, \tag{2.20}$$

Taking the derivative again, the acceleration is defined as,

$$\ddot{\bar{r}}_3 = (\ddot{x} - 2\dot{y} - x)\hat{x} + (\ddot{y} + 2\dot{x} - y)\hat{y} + \ddot{z}\hat{z}, \tag{2.21}$$

Equating Equations (2.21) and (2.17) and inserting the expressions in Equation (2.19), we obtain,

$$\ddot{x} = 2\dot{y} + x - (1-\mu)\frac{x+\mu}{r_{13}^3} - \mu\frac{x-1+\mu}{r_{23}^3}, \tag{2.22}$$

$$\ddot{y} = -2\dot{x} + y - (1-\mu)\frac{y}{r_{13}^3} - \mu\frac{y}{r_{23}^3}, \tag{2.23}$$

$$\ddot{z} = -(1-\mu)\frac{z}{r_{13}^3} - \mu\frac{z}{r_{23}^3}, \tag{2.24}$$

2.1.3. Pseudo-potential function

It is observed that the relations for accelerations show a similar pattern for the three components so, a pseudo-potential function could be defined as,

$$U^* = \frac{1-\mu_e}{r_{13}} + \frac{\mu}{r_{23}} + \frac{x^2+y^2}{2}, \tag{2.25}$$

which satisfies,

$$\begin{cases} \dfrac{\partial U^*}{\partial x} = \ddot{x} - 2\dot{y}, \\ \dfrac{\partial U^*}{\partial y} = \ddot{y} + 2\dot{x}, \\ \dfrac{\partial U^*}{\partial z} = \ddot{z}, \end{cases} \tag{2.26}$$

It follows that,

$$\begin{cases} \dfrac{1}{2}\dfrac{d(\dot{x}^2+\dot{y}^2+\dot{z}^2)}{dt} = \dfrac{dU^*}{dt}, \\ \dfrac{d(2U^*-v^2)}{dt} = 0, \end{cases} \tag{2.27}$$

that is, the model admits one integral of motion, which is called the Jacobi integral. The constant is discovered by German mathematician Carl Jacobi in 1836. Like the energy in the two-body problem, the Jacobi constant is a constant of motion in a restricted three-body problem giving insight into the total energy of the third particle in the rotating frame. It can be defined as,

$$JC = x^2 + y^2 + \frac{2(1-\mu)}{d} + \frac{2\mu}{r} - (\dot{x}^2 + \dot{y}^2 + \dot{z}^2), \tag{2.28}$$

Since the JC is constant along the trajectory, for any given point the possible magnitude of the velocity can be defined from Equation 2.28. Moreover, by equating the velocity terms to 0, the furthest boundary for the trajectory for a particular Jacobi constant can be determined. The boundaries are named zero velocity curves and the regions bounded by these curves are named forbidden zones where the trajectory never passes unless the constant changes. Several of these regions in the Earth-Moon system are visualized in Figure 2.3. It is clearly seen that the forbidden regions are symmetric with respect to the x-axis shrinking with decreasing JC.

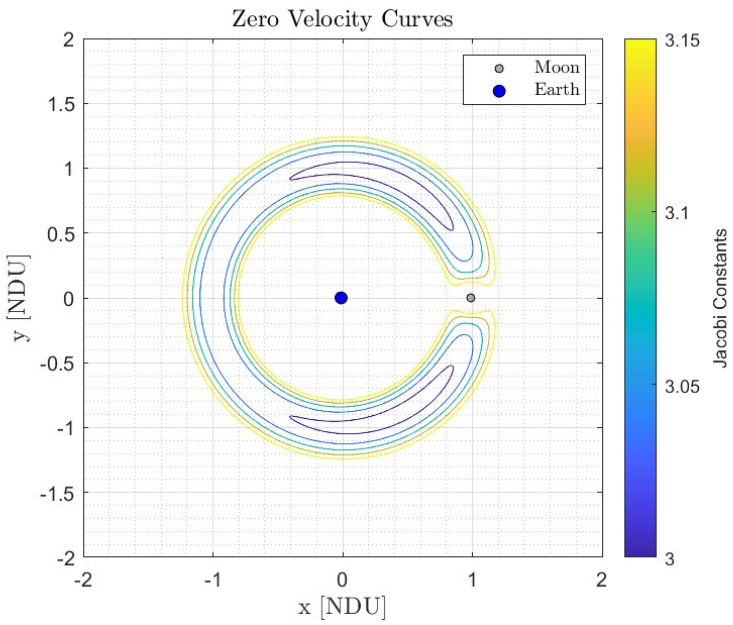

Figure 2.3: Zero velocity curves.

2.1.4. Lagrange points

Due to the nature of the dynamics of a three-body system, there exist five equilibrium points where the third body remains at the same orientation relative to the primaries resulting in zero acceleration and velocity in the rotating frame. Based on these conditions we have,

$$\begin{cases} 0 = x - (1-\mu)\dfrac{x+\mu}{r_{13}^3} - \mu\dfrac{x-1+\mu}{r_{23}^3}, \\ 0 = y - (1-\mu)\dfrac{y}{r_{13}^3} - \mu\dfrac{y}{r_{23}^3}, \\ 0 = -(1-\mu)\dfrac{z}{r_{13}^3} - \mu\dfrac{z}{r_{23}^3}, \end{cases} \tag{2.29}$$

It is observed that the third equation is satisfied only if $z = 0$ hence proving that the equilibrium points are located on the x-y plane. Alternatively, these expressions could be obtained by checking the gradient of the pseudo-potential function as defined in Equation (2.26).

First discovered by Euler in 1765 [28], three of these points lie along the apse line connecting the primaries. The position of these points are found by solving,

$$x = \frac{(1-\mu)}{(x+\mu)^2} - \frac{\mu}{(x-1+\mu)^2}, \tag{2.30}$$

The three roots of Equation (2.30) can be easily found by applying a change of variables as,

$$\begin{cases} x_{L1} = 1 - \mu - \gamma_1, \\ x_{L2} = 1 - \mu + \gamma_2, \\ x_{L3} = -1 - \gamma_3, \end{cases} \tag{2.31}$$

The new variables are inserted into Equation (2.30) and solved numerically for $\gamma_1 > 0$, $\gamma_2 > 0$ and $\gamma_3 > 0$. Here γ_1 designates the distance from the Moon in the direction of Earth. It defines the position of L_1. Similarly, γ_2 describes the distance from the Moon opposite to the direction of Earth defining L_2 point. Finally, γ_3 is used to locate the L_3 where it defines the coordinate $-1 - \gamma_3$ on the x-axis.

First discovered by Lagrange in 1772 [28], the remaining two points are found utilising the first two equations in Equation (2.29). It can be shown that these two relations

are satisfied for $r_{23} = r_{13} = 1$. Hence the remaining two points form two equilateral triangles with respect to the primaries and symmetric with respect to the x-axis. As per the definition, L_4 is positioned above the x-axis and L_5 is located below.

The coordinates for the equilibrium points for the Earth-Moon system are presented in Table 2.2.

Lagrange Point	x $[NDU]$	y $[NDU]$	z $[NDU]$
L_1	0.8369	0	0
L_2	1.1557	0	0
L_3	-1.0051	0	0
L_4	0.4878	0.8660	0
L_5	0.4878	0.8660	0

Table 2.2: Lagrange points for Earth-Moon system.

The location of the equilibrium points along with the zero velocity curves is illustrated in Figure 2.4.

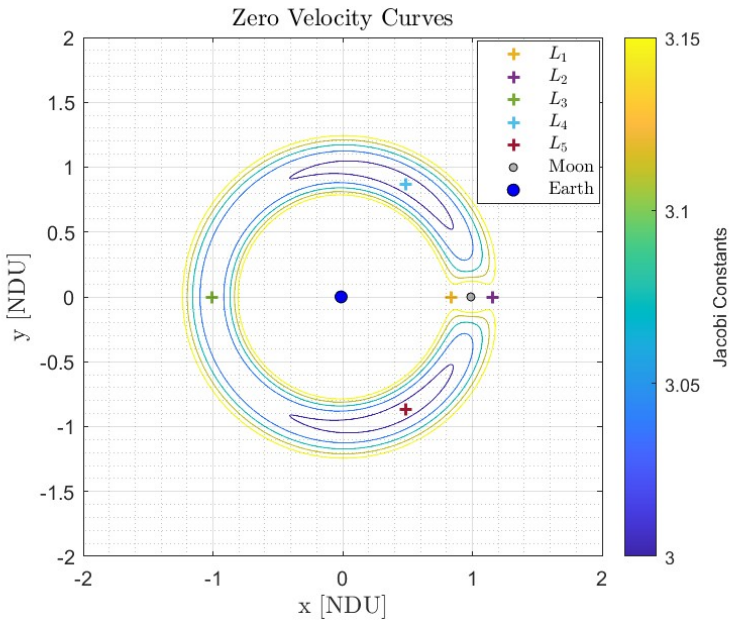

Figure 2.4: Zero velocity curves with equilibrium points.

2.2. Basic numerical methods

2.2.1. Poincaré map

Poincaré map is a useful tool to visualize the behaviour of the dynamic flow of a system. These maps are utilised in many ways such as to find the periodic and quasi-periodic orbit solutions and homoclinic and heteroclinic connections. In this study, two types of planes are selected to be analyzed. Type A defined as the plane defined by $y = 0$ and type B is the plane defined by $x = -\mu$. The sections are visualized in Figure 2.5. Here the maps demonstrate the piercing points of the stable manifold illustrated in Figure 2.6.

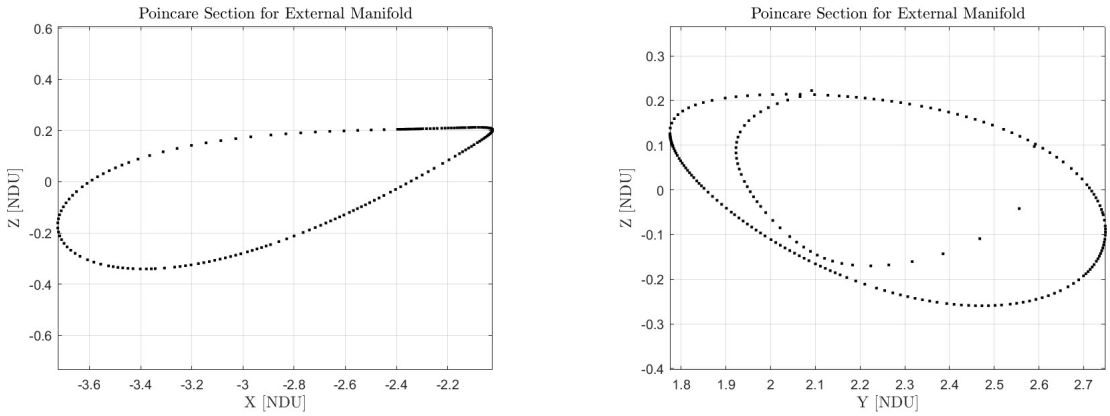

(a) Poincaré section type A $y = 0$.

(b) Poincaré section type B $x = -\mu$.

Figure 2.5: Poincaré section pattern for a stable manifold.

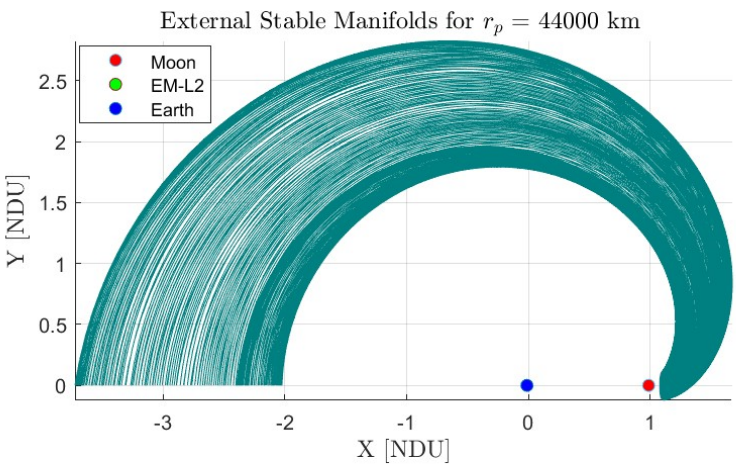

Figure 2.6: Outer stable manifold

2.2.2. State transition matrix

The state transition matrix (STM) is defined as a linear map of the state at t with respect to the state at t_0. It is a very useful tool with many applications. The usages include the targeter design, the definition of the stability behaviour of an orbit, and manifold computation. A specific case of STM is called the monodromy matrix. The monodromy matrix is the STM after one full orbit revolution. The flow of the dynamics system is defined as,

$$\bar{x} = \phi(\bar{x}_0, t_0; t), \tag{2.32}$$

Assuming a small perturbation on a reference solution the flow can be written as,

$$\bar{x} + \delta\bar{x} = \phi(\bar{x}_0 + \delta\bar{x}_0, t_0; t), \tag{2.33}$$

Here a first-order expansion is applied resulting in,

$$\phi(\bar{x}_0 + \delta\bar{x}_0, t_0; t) = \phi(\bar{x}_0, t_0; t) + \frac{\partial\phi}{\partial\bar{x}_0}(\bar{x}_0, t_0; t)\delta\bar{x}_0, \tag{2.34}$$

where inserting Equation (2.33) into Equation (2.34) results in,

$$\bar{x} + \delta\bar{x} = \phi(\bar{x}_0, t_0; t) + \frac{\partial\phi}{\partial\bar{x}_0}(\bar{x}_0, t_0; t)\delta\bar{x}_0, \tag{2.35}$$

Additionally inserting Equation (2.32) into Equation (2.35), the relation of a perturbation at t with respect to the perturbation of the initial state is found as,

$$\delta\bar{x} = \Phi(t, t_0)\delta\bar{x}_0, \tag{2.36}$$

where $\Phi(t, t_0)$ indicates the transition matrix defined as,

$$\Phi(t, t_0) = \frac{\partial\phi}{\partial\bar{x}_0}(\bar{x}_0, t_0; t), \tag{2.37}$$

By definition, at $t = t_0$ the STM is the identity matrix. Having the initial conditions well defined, the STM can be propagated by utilising the system dynamics. Defining the dynamic model as,

$$\dot{\bar{x}} = f(\bar{x}, t), \tag{2.38}$$

The first order Taylor expansion with respect to a reference solution x_* results in,

$$\dot{\bar{x}}(t) = f(\bar{x}_*, t) + \frac{\partial f}{\partial \bar{x}}(\bar{x}_*)(\bar{x} - \bar{x}_*), \tag{2.39}$$

where defining the displacement terms as shown below,

$$\begin{cases} \delta\dot{\bar{x}} = \dot{\bar{x}} - \dot{\bar{x}}_*, \\ \delta\bar{x} = \bar{x} - \bar{x}_*, \end{cases} \tag{2.40}$$

and inserting them and Equation (2.38) into the Equation (2.39). The dynamics regarding the perturbation of the system is found as,

$$\delta\dot{\bar{x}} = A(t)\delta\bar{x}, \tag{2.41}$$

where $A(t)$ is the Jacobian of the system, namely,

$$A(t) = \frac{\partial f}{\partial \bar{x}}(\bar{x}_*), \tag{2.42}$$

Inserting Equation (2.36) into the Equation (2.41), the dynamics of the STM is obtained as,

$$\dot{\Phi}(t, t_0) = A(t)\Phi(t, t_0), \tag{2.43}$$

where $A(t)$ is,

$$A(t) = \begin{bmatrix} 0_{3\times3} & I_{3\times3} \\ U^*_{XX} & 2\Omega \end{bmatrix}, \tag{2.44}$$

where Ω is defined as,

$$\Omega = \begin{bmatrix} 0 & 1 & 0 \\ -1 & 0 & 0 \\ 0 & 0 & 0 \end{bmatrix}, \tag{2.45}$$

In Equation (2.44), the second-order partial derivatives are,

$$U^*_{XX} = \begin{bmatrix} U^*_{xx} & U^*_{xy} & U^*_{xz} \\ U^*_{yx} & U^*_{yy} & U^*_{yz} \\ U^*_{zx} & U^*_{zy} & U^*_{zz} \end{bmatrix}, \tag{2.46}$$

being,

$$\begin{cases} U^*_{xx} = 1 - \dfrac{1-\mu}{r_{13}^3} - \dfrac{\mu}{r_{23}^3} + \dfrac{3(1-\mu)(x+\mu)^2}{r_{13}^5} + \dfrac{3\mu(x-1+\mu)^2}{r_{23}^5}, \\ U^*_{yy} = 1 - \dfrac{1-\mu}{r_{13}^3} - \dfrac{\mu}{r_{23}^3} + \dfrac{3(1-\mu)y^2}{r_{13}^5} + \dfrac{3\mu y^2}{r_{23}^5}, \\ U^*_{zz} = -\dfrac{1-\mu}{r_{13}^3} - \dfrac{\mu}{r_{23}^3} + \dfrac{3(1-\mu)z^2}{r_{13}^5} + \dfrac{3\mu z^2}{r_{23}^5}, \\ U^*_{xy} = \dfrac{3(1-\mu)(x+\mu)y}{r_{13}^5} + \dfrac{3\mu(x-1+\mu)y}{r_{23}^5}, \\ U^*_{xz} = \dfrac{3(1-\mu)(x+\mu)z}{r_{13}^5} + \dfrac{3\mu(x-1+\mu)z}{r_{23}^5}, \\ U^*_{yz} = \dfrac{3(1-\mu)yz}{r_{13}^5} + \dfrac{3\mu yz}{r_{23}^5}, \\ U^*_{yx} = U^*_{xy}, \\ U^*_{zx} = U^*_{xz}, \\ U^*_{yz} = U^*_{yz}, \end{cases} \tag{2.47}$$

2.2.3. Differential corrector

In this study, the trajectory design involves solving a two-point boundary value problem (TPBVP). A differential corrector algorithm is utilised to solve the problem in the CRTBP. Although there are many applicable methods to solve a TPBVP, a simple method based on a Newton approach is utilised for every targeting problem in this thesis due to its basic nature and multiple usages as seen for instance in [20], [15] and [23].

Fixed time targeter

The fixed time differential corrector provides the most basic solution for a TPBVP. Defining an initial state x_0 a transfer trajectory can be defined by a time of flight t as shown in Figure (2.7). The state at the end of the trajectory is shown as $x(t)$. The aim of the algorithm is to find the maneuver Δv_0 such that $x(t) = x_{desired}$.

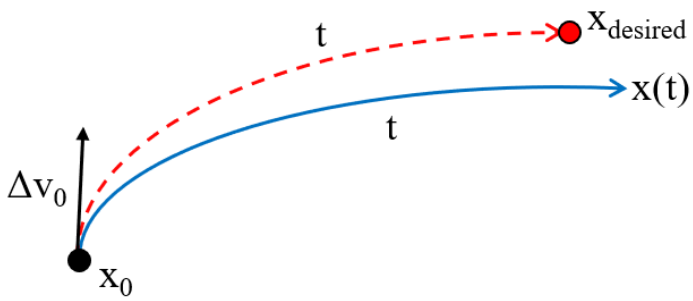

Figure 2.7: Fixed time differential corrector scheme

Since the aim is to target a specific point in the three-dimensional space, Equation (2.48), defines the position errors at the end of propagation.

$$\begin{Bmatrix} \delta x \\ \delta y \\ \delta z \end{Bmatrix} = \begin{Bmatrix} x(t) - x_{desired} \\ y(t) - y_{desired} \\ z(t) - z_{desired} \end{Bmatrix} \tag{2.48}$$

The targeting matrix for the problem is formulated as follows, where the matrix represents the Jacobian of the dynamics flow which is obtained from the STM. Solving the expression for $\partial \dot{x}_0$, $\partial \dot{y}_0$ and $\partial \dot{z}_0$, the initial velocities are updated until $\delta x = \delta y = \delta z \cong 0$.

$$\begin{Bmatrix} \delta x \\ \delta y \\ \delta z \end{Bmatrix} = \begin{bmatrix} \frac{\partial x}{\partial \dot{x}_0} & \frac{\partial x}{\partial \dot{y}_0} & \frac{\partial x}{\partial \dot{z}_0} \\ \frac{\partial y}{\partial \dot{x}_0} & \frac{\partial y}{\partial \dot{y}_0} & \frac{\partial y}{\partial \dot{z}_0} \\ \frac{\partial z}{\partial \dot{x}_0} & \frac{\partial z}{\partial \dot{y}_0} & \frac{\partial z}{\partial \dot{z}_0} \end{bmatrix} \begin{Bmatrix} \delta \dot{x}_0 \\ \delta \dot{y}_0 \\ \delta \dot{z}_0 \end{Bmatrix}, \tag{2.49}$$

Variable time targeter

A more complex alternative for the fixed-time targeter is to introduce the time of flight as a variable for the algorithm. The scheme of the method is illustrated in Figure 2.8 where δt is the change in transfer time.

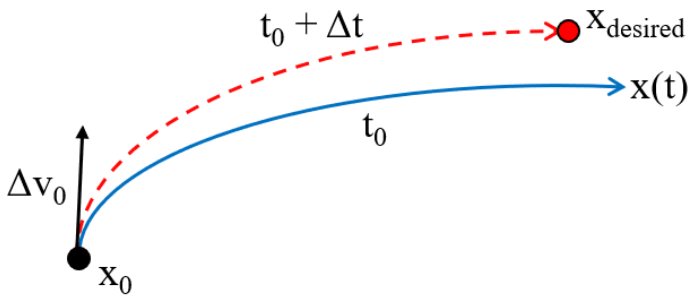

Figure 2.8: Variable time differential corrector scheme

Here the aim of the targeter is the same as the fixed-time case however now the Jacobian matrix has to be updated to include the effect of the time of flight change. The resulting scheme is shown as,

$$\begin{Bmatrix} \delta x \\ \delta y \\ \delta z \end{Bmatrix} = \begin{bmatrix} \frac{\partial x}{\partial \dot{x}_0} & \frac{\partial x}{\partial \dot{y}_0} & \frac{\partial x}{\partial \dot{z}_0} & \ddot{x} \\ \frac{\partial y}{\partial \dot{x}_0} & \frac{\partial y}{\partial \dot{y}_0} & \frac{\partial y}{\partial \dot{z}_0} & \ddot{y} \\ \frac{\partial z}{\partial \dot{x}_0} & \frac{\partial z}{\partial \dot{y}_0} & \frac{\partial z}{\partial \dot{z}_0} & \ddot{z} \end{bmatrix} \begin{Bmatrix} \delta \dot{x}_0 \\ \delta \dot{y}_0 \\ \delta \dot{z}_0 \\ \tau \end{Bmatrix}, \tag{2.50}$$

The resulting Jacobian matrix is 3×4 because there are more free variables than constraints. This results in an infinite number of solutions so a new algorithm is applied that finds the minimum norm solution to the variable-time single-shooting problem. The updated method is,

$$\begin{Bmatrix} \delta \dot{x}_0 \\ \delta \dot{y}_0 \\ \delta \dot{z}_0 \\ \tau \end{Bmatrix} = L^T (LL^T)^{-1} \begin{Bmatrix} \delta x \\ \delta y \\ \delta z \end{Bmatrix} \tag{2.51}$$

where L is the Jacobian matrix, namely, Equation (2.52). Here again, an iterative method is applied to achieve $\delta x = \delta y = \delta z \cong 0$.

$$L = \begin{bmatrix} \frac{\partial x}{\partial \dot{x}_0} & \frac{\partial x}{\partial \dot{y}_0} & \frac{\partial x}{\partial \dot{z}_0} & \ddot{x} \\ \frac{\partial y}{\partial \dot{x}_0} & \frac{\partial y}{\partial \dot{y}_0} & \frac{\partial y}{\partial \dot{z}_0} & \ddot{y} \\ \frac{\partial z}{\partial \dot{x}_0} & \frac{\partial z}{\partial \dot{y}_0} & \frac{\partial z}{\partial \dot{z}_0} & \ddot{z} \end{bmatrix} \tag{2.52}$$

3 | Operational Orbit Design in Earth-Moon L_2

In this chapter, the methodology to generate the family of periodic halo orbits is explained in detail. Then the characteristics of the NRHO family are defined with the demonstration of the eclipse behavior in the Earth-Moon environment.

3.1. Generating Periodic Halo Orbits

One significant behavior of the periodic halo orbits is that they are symmetric with respect to the x-y plane in the rotating frame. Namely, with a careful selection of the initial condition, only three non-zero components exist as defined in,

$$p_0 = [x_0 \ 0 \ z_0 \ 0 \ \dot{y}_0 \ 0]^T, \tag{3.1}$$

To generate a periodic orbit one of these components shall be fixed while the others are iterated until the perpendicular crossing on the x-y plane is achieved at $t = \tau$. In order to achieve the perpendicular crossing, after a half period, the velocity in the x and z direction and the position in y must be equal to zero.

As explained for instance in the [15], since the Halo family bifurcates from the planar Lyapunov family, z_0 is fixed initially. The differential correction procedure aims at finding the roots of the following variations after a time equal to a half period, namely, $t = T/2$,

$$\begin{cases} \Delta y = y(t) - y_0, \\ \Delta \dot{x} = \dot{x}(t) - \dot{x}_0, \\ \Delta \dot{z} = \dot{z}(t) - \dot{z}_0, \end{cases} \tag{3.2}$$

where x_0 and $\dot{y}_0$ are the free variables of the problem varied to achieve the condition $\Delta y = \Delta \dot{x} = \Delta \dot{z} = 0$. Thus the targeting matrix for the problem is defined as,

$$\begin{Bmatrix} \delta y \\ \delta \dot{x} \\ \delta \dot{z} \end{Bmatrix} = \begin{bmatrix} \frac{\partial y}{\partial z_0} & \frac{\partial y}{\partial \dot{y}_0} & \dot{y} \\ \frac{\partial \dot{x}}{\partial z_0} & \frac{\partial \dot{x}}{\partial \dot{y}_0} & \ddot{x} \\ \frac{\partial \dot{z}}{\partial z_0} & \frac{\partial \dot{z}}{\partial \dot{y}_0} & \ddot{z} \end{bmatrix} \begin{Bmatrix} \delta x_0 \\ \delta \dot{y}_0 \\ \delta \tau \end{Bmatrix}, \tag{3.3}$$

Here an iterative procedure is conducted by updating the initial conditions x_0 and $\dot{y}_0$ by subtracting δx_0 and $\delta \dot{y}_0$. The iteration continues until it satisfies the relations $\delta y < \epsilon$, $\delta \dot{x} < \epsilon$, and $\delta \dot{z} < \epsilon$ where ϵ is the tolerance.

A similar process is applied when x_0 is chosen as the fixed component. Now where z_0 and $\dot{y}_0$ are the free variables of the problem varied to achieve the condition $\Delta y = \Delta \dot{x} = \Delta \dot{z} = 0$. The targeting matrix for the problem is defined as,

$$\begin{Bmatrix} \delta y \\ \delta \dot{x} \\ \delta \dot{z} \end{Bmatrix} = \begin{bmatrix} \frac{\partial y}{\partial z_0} & \frac{\partial y}{\partial \dot{y}_0} & \dot{y} \\ \frac{\partial \dot{x}}{\partial z_0} & \frac{\partial \dot{x}}{\partial \dot{y}_0} & \ddot{x} \\ \frac{\partial \dot{z}}{\partial z_0} & \frac{\partial \dot{z}}{\partial \dot{y}_0} & \ddot{z} \end{bmatrix} \begin{Bmatrix} \delta z_0 \\ \delta \dot{y}_0 \\ \delta \tau \end{Bmatrix}, \tag{3.4}$$

where the same iterative procedure is applied until the perpendicular crossing is achieved within a defined tolerance.

To generate the whole orbital family both targeting schemes are used. The selection of the scheme is based on the amount of change of the fixed components x_0 and z_0 where the first method is applied in the regions where z_0 changes in a faster manner and the second method is applied in the regions where x_0 changes in a faster manner.

After the generation of the first orbit, the new initial condition of the Halo orbits can be predicted as,

$$p_{n+1} = p_n + d \cdot q_0, \tag{3.5}$$

here p_{n+1} is the predicted initial state, p_n is the previous initial state, d is scalar defining the magnitude of the increment between the states, and q_0 is the direction of the increment. It has to be noted that the value d is negative for southern families while positive for northern ones. Here the directions are presented as,

$$\begin{cases} q_{0,x} = [1\ 0\ 0\ 0\ 0\ 0]^T, \\ q_{0,z} = [0\ 0\ 1\ 0\ 0\ 0]^T, \end{cases} \tag{3.6}$$

In the beginning, we fix z_0, then when expression (3.7) holds, then we switch to the

algorithm where x_0 is the fixed parameter.

$$|x_0^n - x_0^{n-1}| > |z_0^n - z_0^{n-1}|, \tag{3.7}$$

Having found the initial states for the whole family, the complete periodic orbit can be obtained by propagating the first state by 2τ. Also to save computational time, the mirror image of the half orbit can be found as well since the periodic orbits are symmetric with respect to the x-y plane.

3.2. Halo and NRHO families

Our main target, the NRHOs, are periodic orbits and belong to the halo family. So starting from a planar Lyapunov orbit, Halo orbits are generated up to a perilune of 50 km for both northern and southern counterparts. The initial state for the first periodic orbit is given in Table 3.1. The magnitude of the increment d is selected as 0.001.

x_0 $[NDU]$	y_0 $[NDU]$	z_0 $[NDU]$	$\dot{x}_0$ $[NDU]$	$\dot{y}_0$ $[NDU]$	$\dot{z}_0$ $[NDU]$	T $[NDU]$
1.1809	0	-0.0001	0	-0.1558	0	3.4155

Table 3.1: Initial state for $EM - L_2$ Halo family generation.

The results are presented in Figure 3.1 and 3.2 where the green dot indicates the EM-L2 while the red dot represents the Moon.

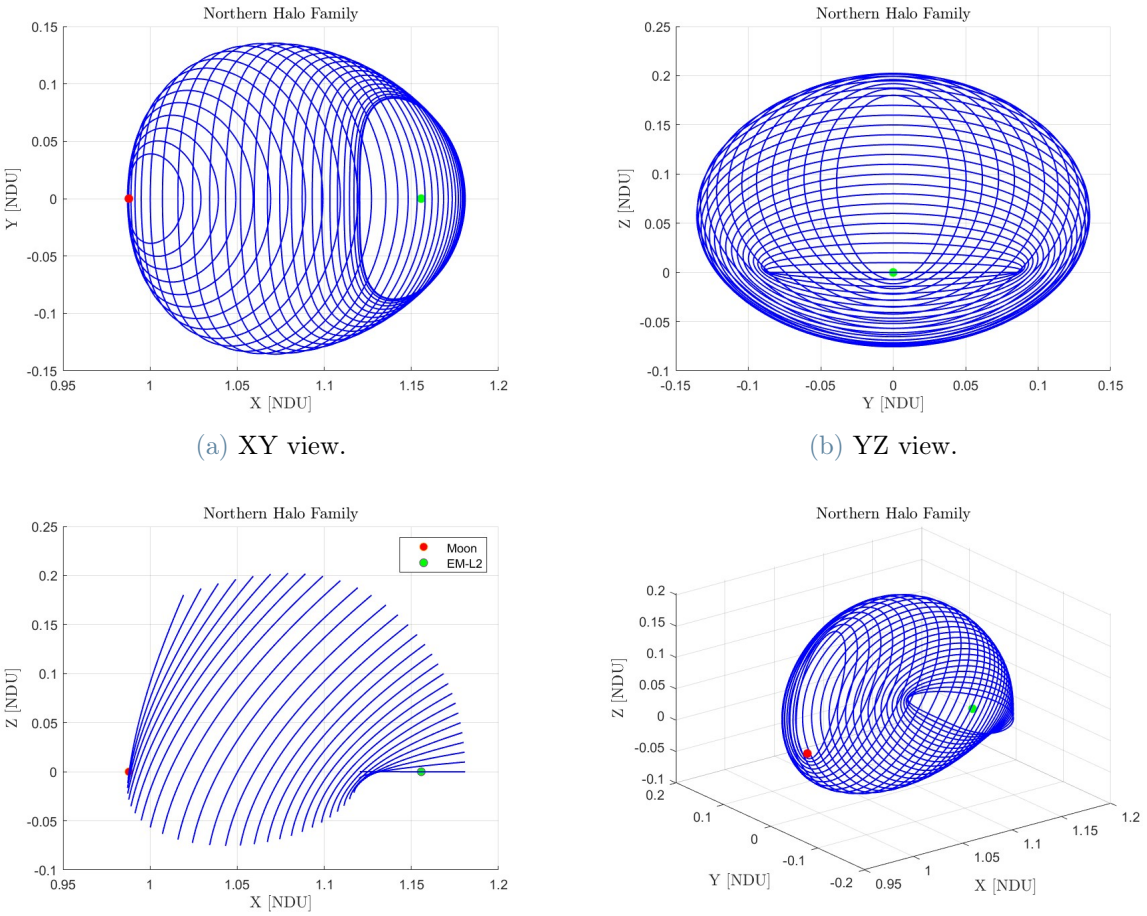

(a) XY view.

(b) YZ view.

(c) XZ view.

(d) XYZ view.

Figure 3.1: Northern $EM - L_2$ halo families.

Since the motion is symmetric along the x-y plane, there are northern and southern Halo solutions that bifurcate from the same Lyapunov orbit. As explained before, southern families are obtained by incrementing the initial states in the negative z-direction.

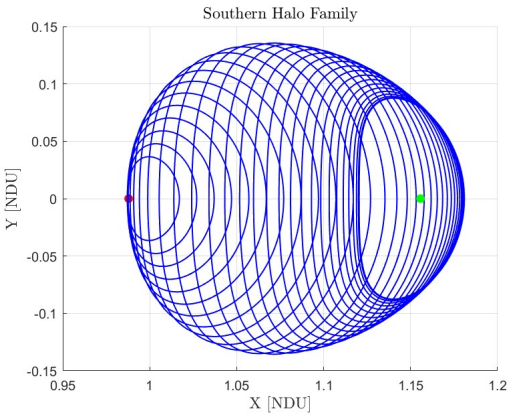

(a) XY view.

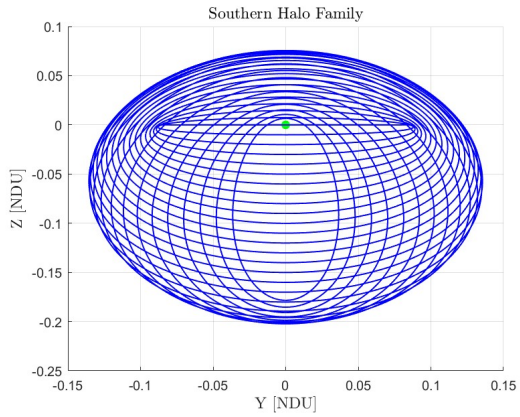

(b) YZ view.

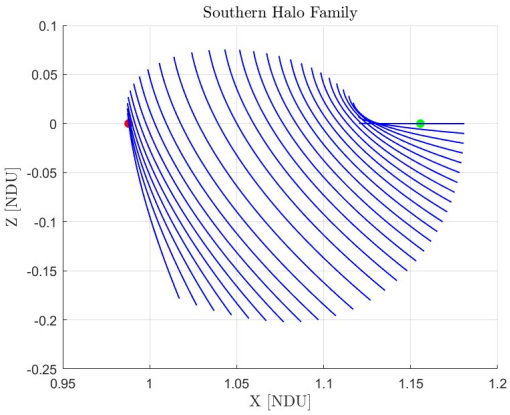

(c) XZ view.

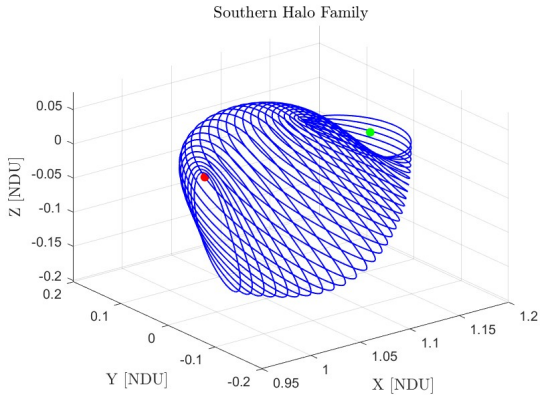

(d) XYZ view.

Figure 3.2: Southern $EM - L_2$ halo families.

As previously stated NRHOs are a subfamily of halo orbits. The classification is based on a parameter called the stability index. The index is based on the eigenvalues of the monodromy matrix and indicates the stability property of the orbit, as defined in Equation (3.8),

$$v = \frac{1}{2}\left(|\lambda_1| + |\lambda_2|\right), \tag{3.8}$$

Here λ_1 is the real eigenvalue greater than 1 and λ_2 is the real eigenvalue lower than 1. Based on the value of the stability index v, the system is: stable (v<1), unstable (v >1), or marginally stable ($v = 1$). In Figure 3.3, the evolution of the stability index as a function of the perilune is shown for the southern family of halos. As we can see with decreasing perilune, the stability index rapidly converges. The magnified part of the plot shows the range where the NRHOs are usually defined. The orbits in this region are more

stable compared to the other Halo orbits thus providing advantageous station-keeping properties.

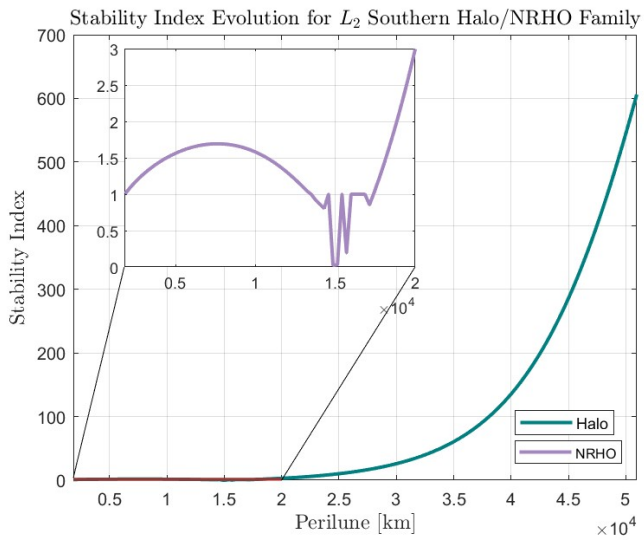

Figure 3.3: Stability index as a function of the perilune radius for the L2 southern family of halos.

Additionally, in Figure 3.4a and 3.4b, the period and Jacobi constant evolution are provided. The period of NRHOs ranges between 6-10 days around the Moon increasing with higher perilune. The behavior is quite the opposite for the Jacobi constant in the NRHO part where higher perilune indicates a lower value.

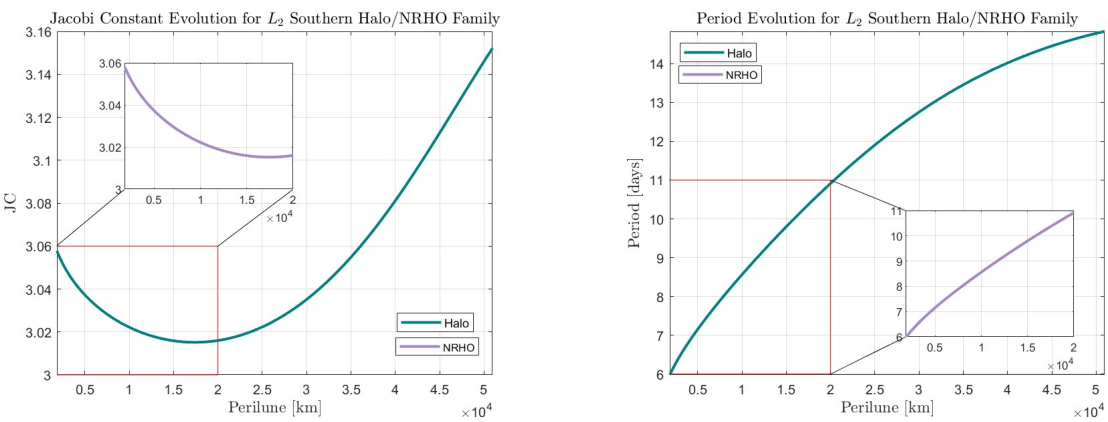

(a) Jacobi constant. (b) Period.

Figure 3.4: Jacobi constant and period as a function of the perilune radius for the L2 southern family of halos.

Like Figure 3.1 and 3.2, in Figure 3.5 and Figure 3.6 we have plotted the NRHO families

of both northern and southern families in a tighter manner. Here we have also shown the stability behavior by using a color map.

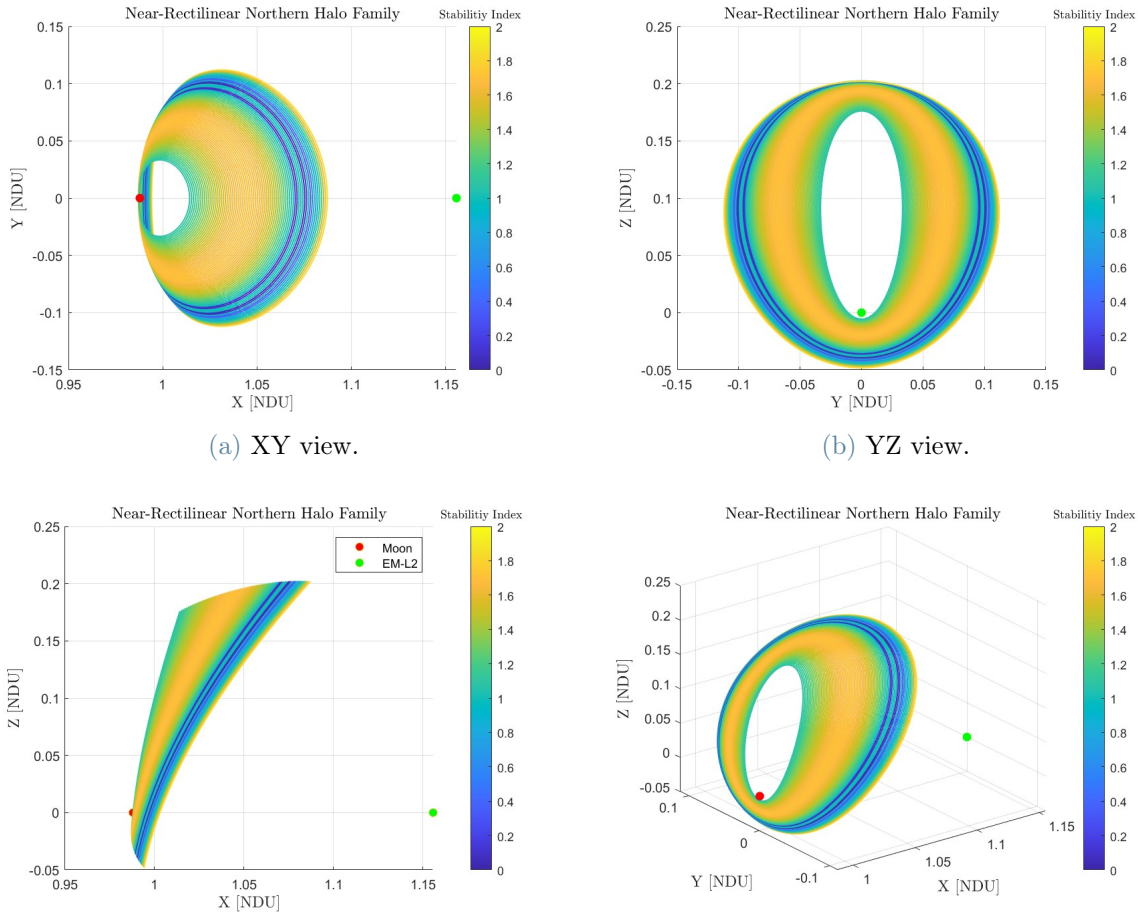

(a) XY view.

(b) YZ view.

(c) XZ view.

(d) XYZ view.

Figure 3.5: Northern $EM - L_2$ NRHO families.

Comparing Figure 3.5 and 3.6, the stability behavior is quite similar for both northern and southern family members.

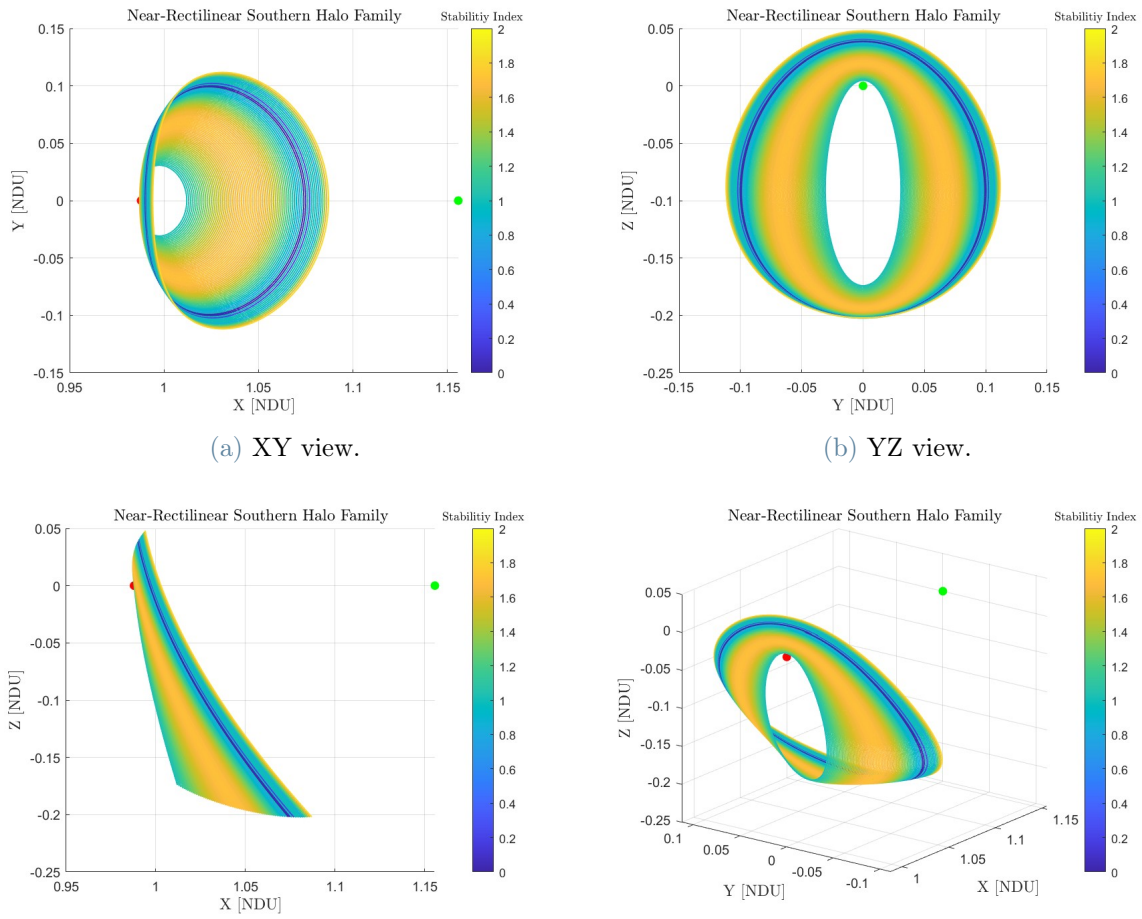

(a) XY view.

(b) YZ view.

(c) XZ view.

(d) XYZ view.

Figure 3.6: Southern $EM - L_2$ NRHO families.

3.3. Eclipse analysis for EM-L2 NRHO family

The eclipse behavior of the NRHO family is modeled and analyzed thoroughly. The eclipse occurs if a body blocks the light rays coming from an illuminating body. For the spacecraft design, the eclipse duration is a critical parameter that produces inputs for the solar array design and thermal requirements. Regarding the mission analysis, it is also crucial to be aware of the eclipse durations to consider the absence of solar radiation pressure affecting the station-keeping requirements. In order to conduct the analysis the Sun is introduced in the Earth-Moon rotating frame as illustrated in Figure 3.7.

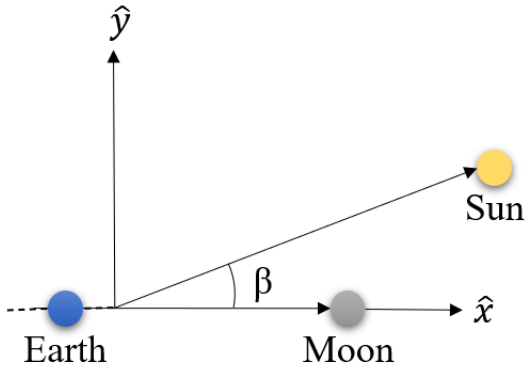

Figure 3.7: Sun placement in the rotating frame.

The Sun is assumed to be located at a distance of 1 AU from the center of the rotating frame following a circular orbit with an inclination of 5 degrees. The method is based on the study [21] which focuses on the $EM - L_1$ halo orbits. Additionally in [32] has studied eclipse characteristics of $EM - L_2$ NRHOs as well. At $t = 0$ the Sun is located behind of the Moon resulting in a full solar eclipse. Then the Sun phase angle β is defined between the solar vector and the x axis of the rotating frame. The phase angle is incremented by 1 degree at every step in order to simulate all possible Sun-Earth-Moon geometries for one year. At each step, the NRHO is propagated for one full period along with the Sun phase angle thus simulating the behavior of the illuminating body for one complete orbit.

3.3.1. The definitions of shadow regions

To have a clear approximation of the eclipse time a shadow model is selected for the mission analysis. The shadow model is based on a basic geometrical analysis presented in [29]. Instantaneous change along the shadow regions is assumed. The geometry of the problem is presented in Figure 3.8.

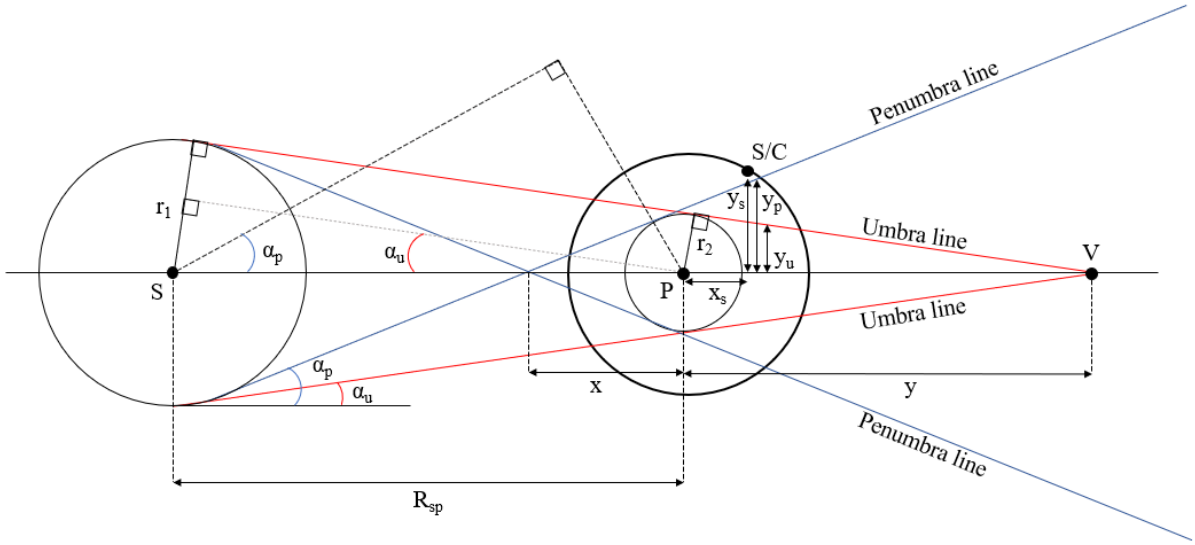

Figure 3.8: Eclipse geometry.

Here the area between the penumbra and umbra line defines the region where the partial eclipse occurs whereas the region between the umbra lines defines the full eclipse event. Both primaries are assumed to have a spherical geometry. The illuminating body is centered at point S having a radius of r_1 and the eclipsing body is centered on point P with a radius of r_2. The satellite follows an orbit around the eclipsing body represented by a thick black line. The distance to the apse line connecting the primaries is represented as y_s and the vertical distance of the umbra and penumbra line at the satellite position is defined as y_u and y_p, respectively. The illumination state of the spacecraft could be obtained by comparing the y_s with y_p and y_u such that the $y_u < y_s < y_p$ indicates partial eclipse and $y_s < y_u$ shows that the satellite is in the umbra. Definition of the y_p and y_u are,

$$\begin{cases} y_p = \tan(\alpha_p)(x + x_s), \\ y_u = \tan(\alpha_u)(y - x_s) \end{cases} \tag{3.9}$$

where α_p and α_u are the angles of penumbra and umbra, respectively. It is clearly observed that the umbra vertical line shrinks while the penumbra line increases. The angles of penumbra and umbra could be found as,

$$\begin{cases} \sin(\alpha_p) = \dfrac{r_1 + r_2}{R_{sp}}, \\ \sin(\alpha_u) = \dfrac{r_1 - r_2}{R_{sp}}, \end{cases} \tag{3.10}$$

where R_{sp} is the distance between the primaries. The resulting angles for the Sun-Earth and Sun-Moon couple are presented in Table 3.2,

Eclipsing Body	α_p $[deg]$	α_u $[deg]$
Earth	0.269007205	0.264121687
Moon	0.267227	0.265896

Table 3.2: Penumbra and umbra angles for primaries.

3.3.2. Eclipse analysis results

Figure 3.9 shows the eclipse behavior of the NRHO family with respect to β. In Figure 3.9a and 3.9c, the color bar indicates the duration of eclipse for one revolution in hours whereas in Figure 3.9b and 3.9d, it indicates the percentage of the eclipse duration with respect to the orbital period of the NRHO. It is clearly seen that no conjoined eclipse occurs with the Moon and Earth at the same geometry.

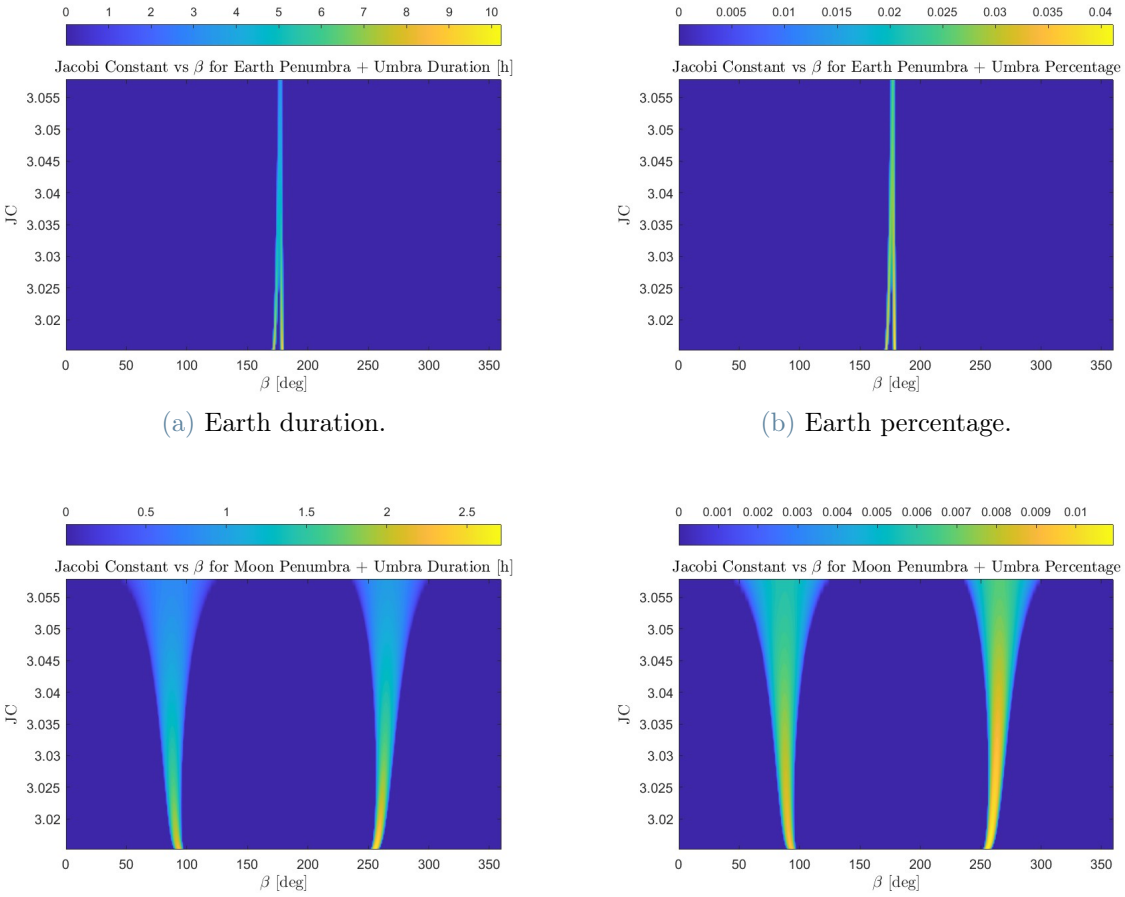

(a) Earth duration.

(b) Earth percentage.

(c) Moon duration.

(d) Moon percentage.

Figure 3.9: Eclipse behaviour due to primaries.

Starting with the Earth, in Figure 3.9a and 3.9b, it is observed that the eclipse occurs only for a small range of Sun phase angles around 180 degrees. Along the vertical axis, it is seen that for Jacobi constant ranges from 3.035 to 3.055, the orbit experiences eclipses for a single range of β within a year whereas, for the lower Jacobi constants, there are two sets of ranges. The maximum eclipse duration is found as 10 hours corresponding to 0.04% of the full period for $JC = 3.015$ and $\beta = 179$ degrees.

For the Moon, the behavior is quite different compared to the Earth, as seen in Figure 3.9c and 3.9d. It is observed that the variation in the eclipse range of the Sun phase angle is highly dependent on the NRHO selection with a lower Jacobi constant corresponding to a lower range of β. Here, on contrary to the Earth there are always two sets of ranges for all JC options. The maximum eclipse time due to the Moon is computed as 2.7 hours corresponding to 0.011% of the full period for again $JC = 3.015$ and $\beta = 255$ degrees.

As shown before in Figure 3.4a, a higher Jacobi constant indicates a lower perilune. As a result, it is concluded for the Moon, closer orbits experience the eclipse in a shorter duration per orbit but for a wider range of Sun phase angles.

In Figure 3.10, the eclipse evolution of a NRHO with 17400 km perilune has been presented for the Moon and Earth showing clearly the phase angles when the satellite enters the shadow regions.

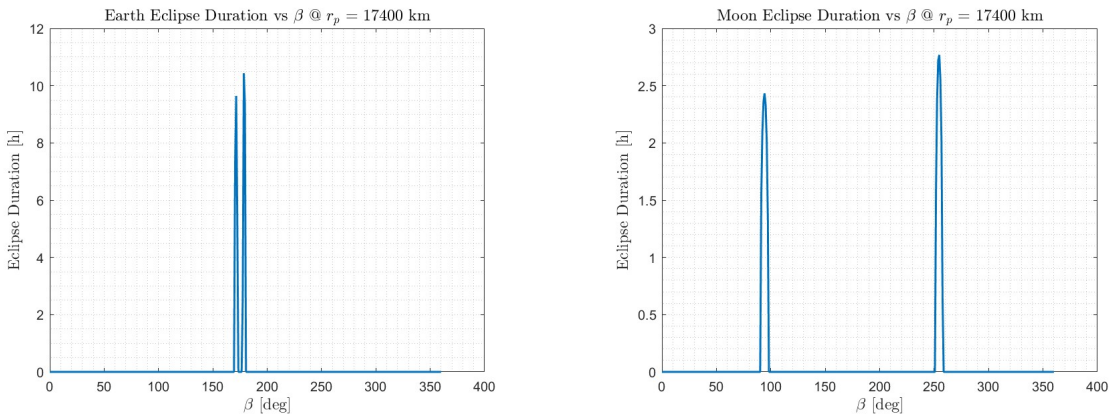

(a) Earth. (b) Moon.

Figure 3.10: 1 year eclipse behaviour.

Figure 3.11 demonstrates the maximum eclipse scenarios for one full period due to the primaries, showing that for both Earth and Moon, it occurs for the orbit with perilune 17400 km. The phase angle corresponding to Earth is $\beta = 179$ and for the Moon, it is $\beta = 255$ degrees.

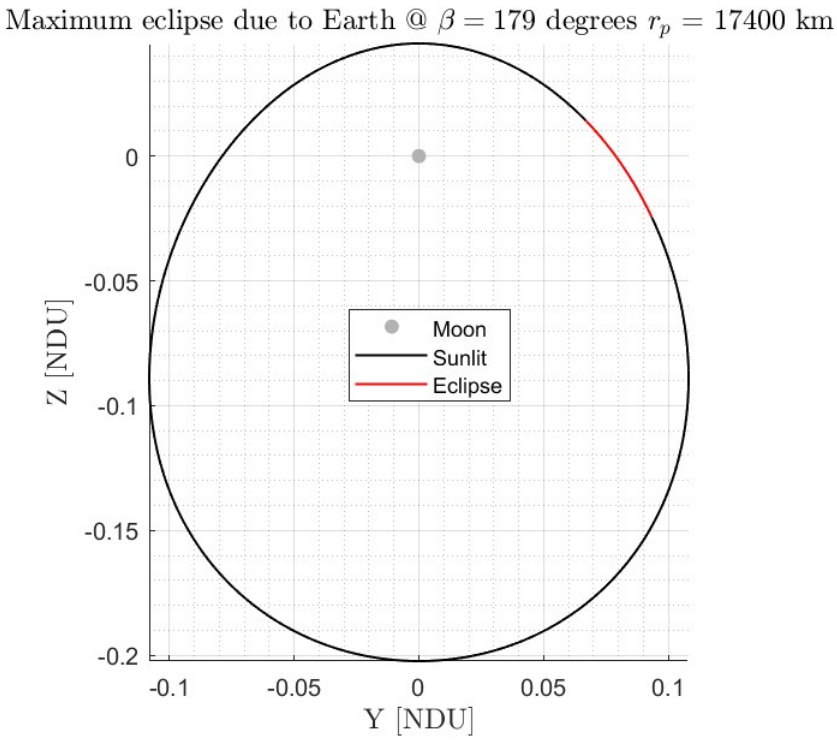

(a) Earth.

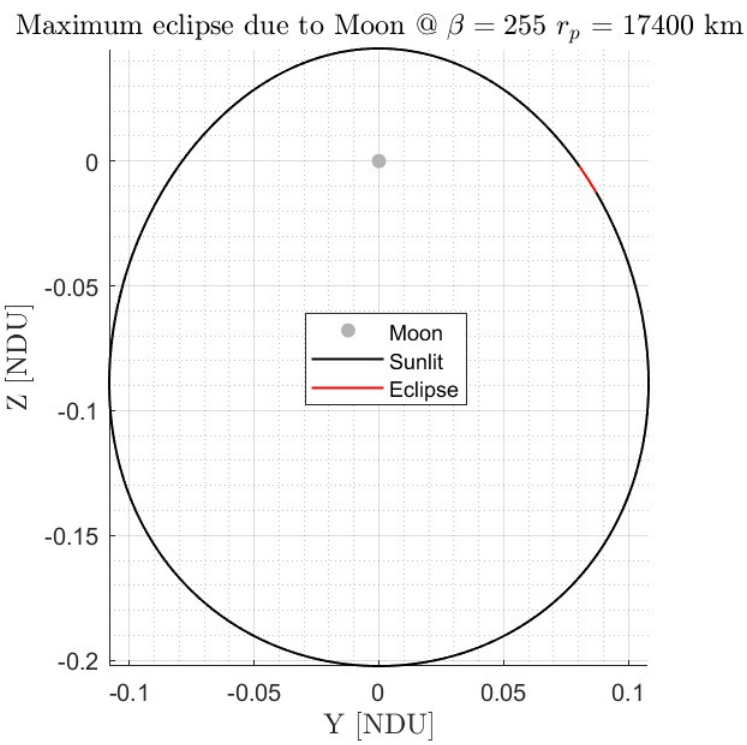

(b) Moon.

Figure 3.11: Maximum eclipse orbits.

In Figure 3.12 the total eclipse time for one year for each NRHO orbit has been presented. It is clearly seen that the eclipse due to the Moon decreases sharply up to 8000 km of perilune radius while eclipsing due to Earth increases in a nearly steady manner. When the sum of two bodies is considered after 3000 km the overall eclipse duration remains steady at around 70 hours per year. The maximum duration is 94 hours for the Moon corresponding to a NRHO with 2000 km perilune whereas for the Earth it is around 45 hours with a perilune of 17000 km.

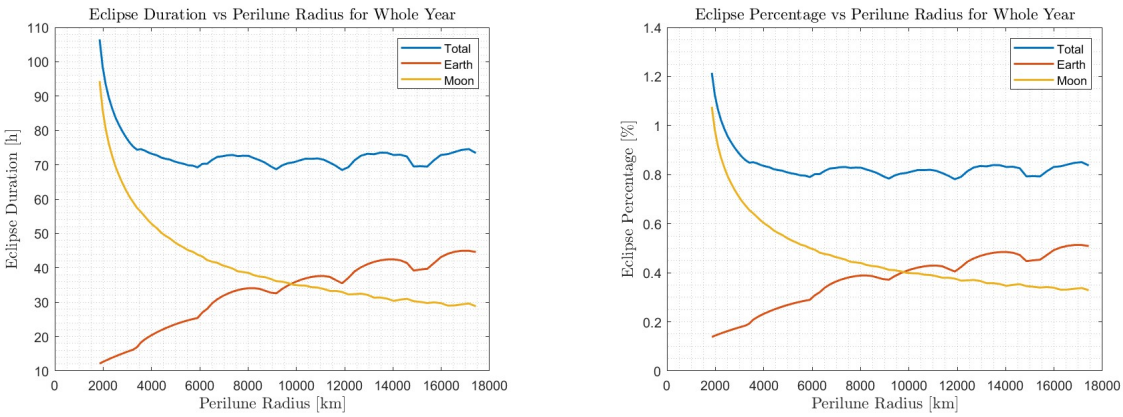

(a) Duration. (b) Percentage.

Figure 3.12: 1 year total eclipse behaviour.

4 | Parking Orbit to Halo Transfer Trajectory Design

In this chapter, the detailed description of the transfer trajectory design from a given Earth parking orbit to a given halo orbit is explained. The trajectory involves three segments: halo inner stable manifold, transfer to the stable manifold, and the parking orbit. First of all, the method to obtain the manifolds is demonstrated. Secondly, the possible parking orbit selections are presented. Thirdly, as a preliminary approach, the Hohmann transfer design is analyzed illustrating the behavior of various Poincaré sections and parking orbit types. Finally, based on the previous results, the trajectory design is refined for the stable manifold transfer, and the parking orbit by implementing a targeting algorithm in the CRTBP. A similar study is conducted in [3] and [14] targeting Halo orbits around $EM - L_2$ while in [2] the invariant manifolds are utilized to target Lissajous orbits at $EM - L_1$.

4.1. Computing manifolds

As mentioned before, the periodic around the equilibrium points have stable, unstable, or marginally stable characteristics [27]. A useful and important characteristic of these unstable orbits is the existence of trajectories that approach and depart from the periodic orbit asymptotically. The two sets of trajectories are called hyperbolic invariant manifolds where the "invariant" definition comes from the fact that if a spacecraft is placed on the manifold, it will remain on the manifold through the propagation [8]. The computation of these manifolds involves the utilization of a monodromy matrix corresponding to a given periodic orbit. The matrix provides insight into the stability behavior of the state by its eigenvalues and eigenvectors. The eigenvector corresponding to the real eigenvalue lower than 1 is used to find a linear approximation of the stable manifold, whereas the eigenvector corresponding to the real eigenvalue greater than 1 is used to compute an initial condition on the unstable manifold. Each hyperbolic manifold has two branches, a positive and a negative one. In order to obtain stable manifolds backward propagation in

time is required while forward in time is required for unstable manifolds [19]. The local perturbed state can be computed as,

$$\bar{X}_s = \bar{x}(t_i) + d \cdot \bar{V}^{W_s}(t_i) \tag{4.1}$$

Here, $x(t_i)$ is the state at time t_i on the halo orbit, d is a scalar indicating the magnitude of the perturbation and $\bar{V}^{W_s}(t_i)$ is the normalized stable eigenvector indicating the direction of the perturbation. As suggested in [23], for Earth-Moon systems the perturbations ranging from 30 - 70 km is sufficient to hold the linear approximation. In [23] study the eigenvectors are normalized with respect to the first three elements such that the perturbed state is at a constant distance at every point. The resulting perturbation is on the order of 0.1 m/s. In this study, normalization is conducted for all of the components of the eigenvector. An intermediate value of 50 is selected for the perturbation, resulting in position perturbation in the range of 10 to 30 km and in a velocity perturbation of nearly 0.1 m/s. It is observed that both of the methods are feasible for the generation of the manifolds. The normalized vector is,

$$\bar{V}^{W_s}(t_i) = \frac{\hat{Y}^{W_s}(t_i)}{|\hat{Y}^{W_s}(t_i)|} \tag{4.2}$$

The local stable eigenvector $\hat{Y}^{W_s}(t_i)$ consists of six elements as shown below,

$$\hat{Y}^{W_s}(t_i) = [x_s \ y_s \ z_s \ \dot{x}_s \ \dot{y}_s \ \dot{z}_s]^T \tag{4.3}$$

The same procedure applies when computing the local unstable perturbed state as,

$$\bar{X}_u = \bar{x}(t_i) + d \cdot \bar{V}^{W_u}(t_i) \tag{4.4}$$

where $\bar{V}^{W_u}(t_i)$ defined as,

$$\bar{V}^{W_u}(t_i) = \frac{\hat{Y}^{W_u}(t_i)}{|\hat{Y}^{W_u}(t_i)|} \tag{4.5}$$

and $\hat{Y}^{W_u}(t_i)$ is,

$$\hat{Y}^{W_u}(t_i) = [x_u \ y_u \ z_u \ \dot{x}_u \ \dot{y}_u \ \dot{z}_u]^T \tag{4.6}$$

To compute the local manifolds, the knowledge of the corresponding stable eigenvector is required. There are two ways to obtain this vector. The first way is to compute the

monodromy matrix corresponding to each state along the periodic orbit resulting in a computationally demanding process. There are ways to reduce the process by obtaining the state transition matrix at the half period and estimating the monodromy matrix as explained in detail in [23]. The other way is to utilize the STM to approximate the local eigenvector by multiplying it with the stable eigenvector at the initial state. Then the local unstable eigenvector is computed as,

$$\hat{Y}_i^{W_u} = \Phi(t_i, t_0)\hat{Y}_0^{W_u} \tag{4.7}$$

The local stable eigenvector is computed as,

$$\hat{Y}_i^{W_s} = \Phi(t_i, t_0)\hat{Y}_0^{W_s} \tag{4.8}$$

In Figure 4.1 stable and unstable manifolds of a Halo orbit are presented,

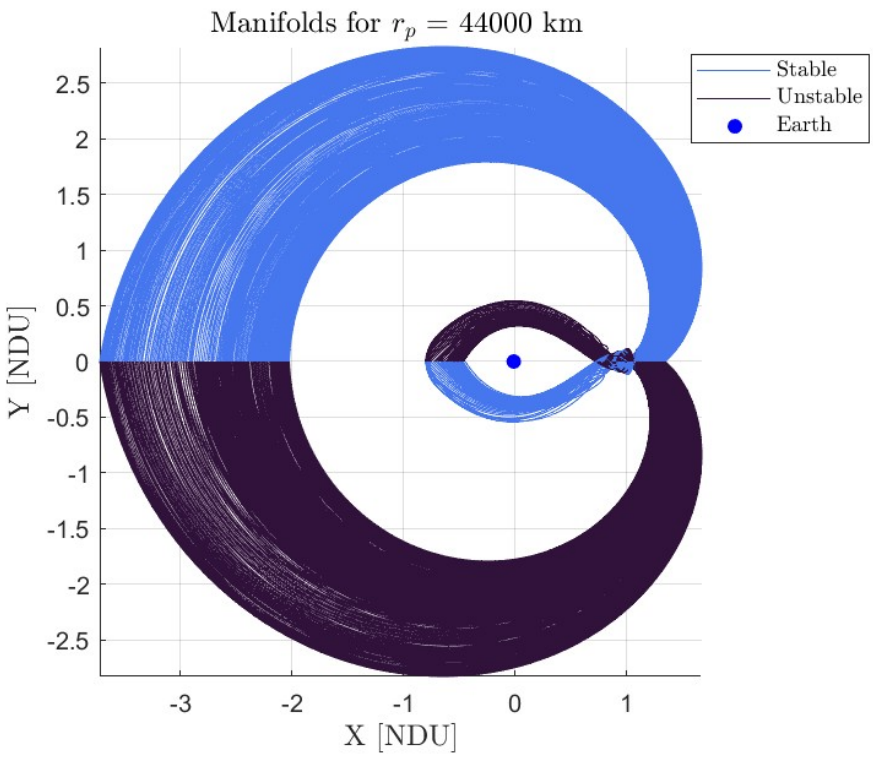

Figure 4.1: Manifolds for Halo in Earth-Moon system.

As stated before, in order to obtain the global stable manifolds a backward propagation in time is required, and forward in time for global unstable manifolds. Here it is important to check during the propagation of a possible Moon impact scenario such that filtering is

required. Additionally, it is observed that within the Earth-Moon CRTBP, there are no feasible interior manifolds below 320000 km of perilune radius. Plus no manifolds exist for NRHO orbits that are stable so a transfer scenario involving these types of Halos and NRHOs is not possible with the provided mission scheme.

4.2. Earth parking orbit design

In order to observe the effect of the parking orbit selection on the total Δv cost, various options are analyzed. In this study, the shape of the parking orbits is fixed by assuming circular LEO and GTO options with perigee altitudes ranging from 200 - 2000 km. No constraints are imposed regarding the orientation of the parking orbit.

4.2.1. LEO to GTO transfer

In order to quantify a possible parking orbit change, a preliminary analysis regarding Δv cost to reach GTO from LEO has been conducted. GTO orbit is achieved by a Hohmann transfer. Equation (4.9) gives the required Δv:

$$\Delta v = \sqrt{\frac{\mu}{r_1}}\left(\sqrt{\frac{2r_2}{r_1+r_2}} - 1\right) \tag{4.9}$$

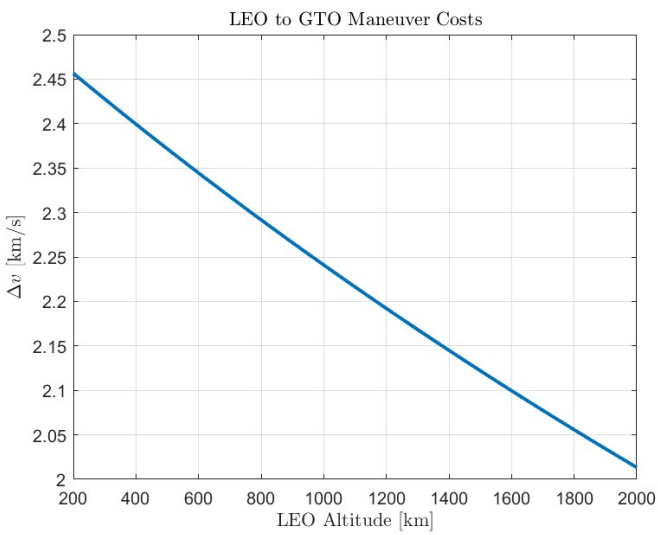

Figure 4.2: Required Δv to reach GTO from LEO.

where μ is the standard gravitational parameter of Earth, r_1 is the perigee of transfer orbit, r_2 is apogee of the target orbit. The perigee is selected as the altitude of the LEO, while

the apogee is selected as the generic altitude of the Geostationary Earth Orbit (GEO). The resulting total Δv of the maneuver is presented in Figure 4.2. The Δv ranges between 2.4 - 2.0 km/s, decreasing with increasing LEO altitude.

4.3. Parking orbit to manifold insertion

In this study with the specified Poincaré section in Chapter 2 , it is observed that within the 1-year time limit imposed on the propagation of the manifolds, the trajectories do not pass close to the Earth so an intermediate transfer is required between the parking orbit and the stable manifold.

4.3.1. Hohmann maneuver approach

As a preliminary approach, by utilizing the two-body dynamics, a Hohmann-like procedure is applied between the parking orbit and the point of intersection of the manifold with a given Poincaré section in order to see the effect of the various Poincaré sections and parking orbit candidates regarding total maneuver cost. The method involves two impulsive burns at the apogee and the perigee of the transfer orbit. The apogee is defined as the manifold piercing point at the Poincaré map whereas the perigee corresponds to the perigee of the parking orbit. Here, the parking orbit is assumed to be perfectly aligned with the transfer trajectory thus not considering any Δv requirement for the inclination correction. Equation (4.9) is used to compute the Δv_{TLI} while Δv_{INS} is obtained by taking the difference of the velocity at the apogee of the transfer orbit and manifold state at Poincaré section.

The manifold computation is conducted in the range of 32000 to 50000 km perilune radius incrementing the perilune radius by 2000 km. Additionally, for the analysis, 500 points are selected on the Halo orbit.

At first, Poincaré section A is analyzed in detail. In Figure 4.3, the total maneuver cost for 44000 and 46000 km perilune radius Halo is presented utilizing a GTO as parking orbit. The cost of the transfer ranges between 0.65 to 1.6 km/s for the first option while the range is between 0.65 to 1.7 km/s for the second option. It is observed that for both options the total Δv reduces in a linear manner with increasing apogee radius up to 300000 km for all possible perigee options, thus suggesting an optimal choice for the selection of the trajectory. This pattern is observed for the whole Halo family. Furthermore, it is demonstrated that the selection of a lower parking orbit perigee results in an overall less Δv for both Halo. As seen in the magnified images in Figure 4.3a, nearly 100 m/s of cost

reduction could be achieved if the 200 km option is selected instead of 2000 km. The same conclusion is obtained for the 46000 km option as well, demonstrating a 100 m/s reduction of transfer for properly selected perigee.

Looking at Figure 4.4, the behavior of Δv_{TLI} and Δv_{INS} are observed for a GTO orbit with various perigee altitudes. Comparing Figures 4.3 and 4.4a, it is seen that the overall pattern of Δv_{TOT} is dominated by the Halo insertion maneuver. The insertion maneuver ranges between nearly 0 to 1.1 km/s showing an optimum point at the apogee radius at nearly 300000 km. Contrary to the total cost plot, it is seen that the higher perigee results in an overall lower insertion maneuver for the same apogee radius, suggesting a 50 m/s difference between the maximum and minimum perigee options. As illustrated in Figure 4.4b, the variation of the injection maneuver is significantly less compared to the insertion maneuver. For a particular perigee, the Δv varies nearly 0.2 km/s increasing with higher apogee. Additionally, the vertical distribution of points suggests that the injection maneuver varies by 50 m/s between the possible parking altitudes.

Having a robust idea of the possible GTO options, now LEO options are presented. As illustrated in Figure 4.5, It is seen that, compared to GTO, the perigee variation results in a much greater total Δv for the same apogee radius, ranging up to 400 m/s. Similar to the previous GTOs the linear behavior is also observed for both Halo orbits presented again suggesting a minimum cost near 300000 km of apogee radius. As illustrated in Figure 4.5a and 4.5b, the lowest possible options are 2.8 and 2.7 km/s for the 44000 and 46000 km perilune case respectively. The main difference compared to is regarding the selection of the optimal altitude. As both figures suggest a higher parking orbit altitude is much more efficient, saving nearly 400 m/s.

The insertion and injection analysis for the LEO options is illustrated in Figure 4.6. As clearly seen in Figure 4.6a the insertion maneuver shows a distribution the same as the GTO case ranging between 0 to 1.1 km/s demonstrating again a linear distribution with a minimum point. For Δv_{TLI}, Figure 4.6b suggests that the variation in the distance of the insertion point is only providing a maximum cost saving up to 100 m/s whereas the variation of the perigee altitude causes a significant variation of 400 m/s.

As suggested before, the Poincaré section B is also analyzed for possible low-cost transfers. The total Δv cost for GTO and LEO options is presented in Figure 4.7. It is seen in Figure 4.7a that the Δv distribution for GTO is much narrow with varying perigee altitude compared to the type B case, demonstrating a maximum change up to 40 m/s. This variation is significantly higher in the LEO case as illustrated in Figure 4.7b, resulting in a nearly 500 m/s difference between 200 km and 2000 km orbit radius selection. Both

results suggest that the Type B Poincaré section shows a rather linear decreasing behavior with an increasing apogee radius with the lowest possible Δv nearly 1.2 km/s for GTO and 3.2 km/s for LEO. It is clear that for the Type B Poincaré section, the resulting maneuver costs are higher thus no further detailed analysis is conducted.

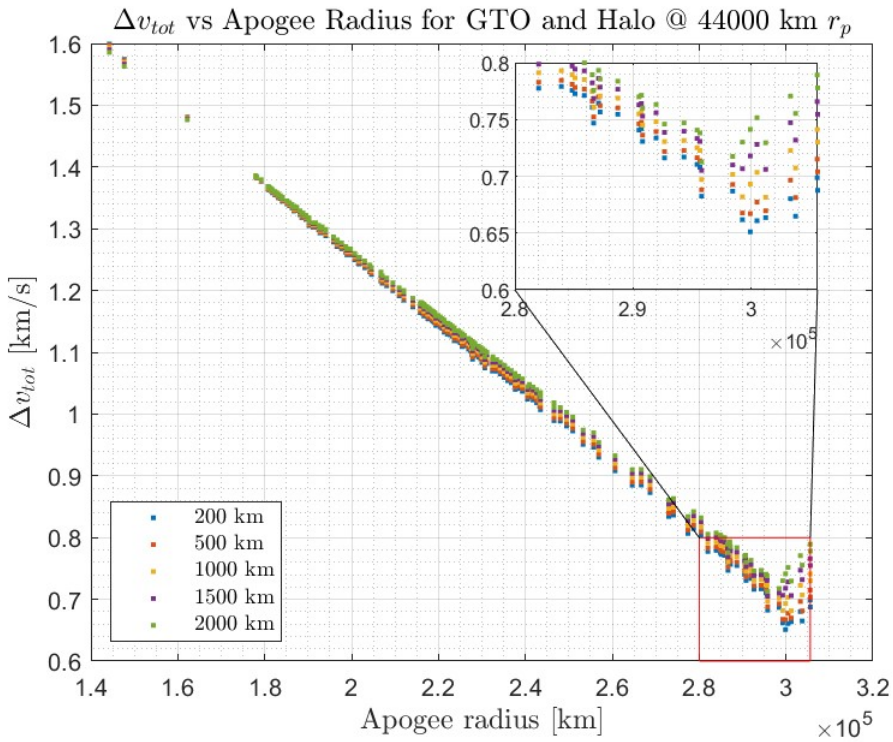

(a) $r_p = 44000$ km .

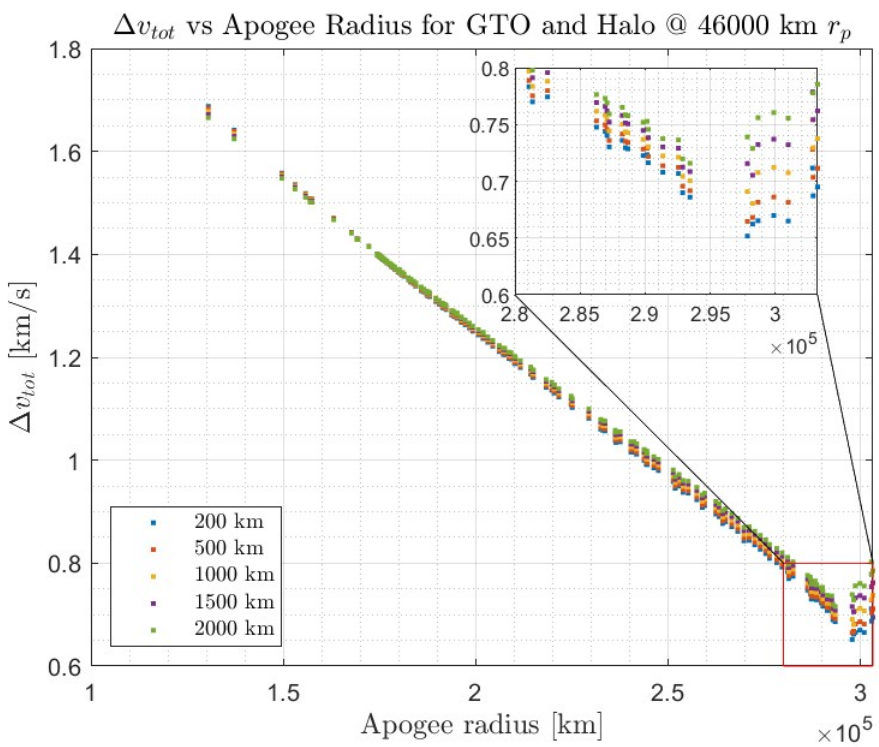

(b) $r_p = 46000$ km.

Figure 4.3: Total Δv cost for different Halo with GTO as parking orbit.

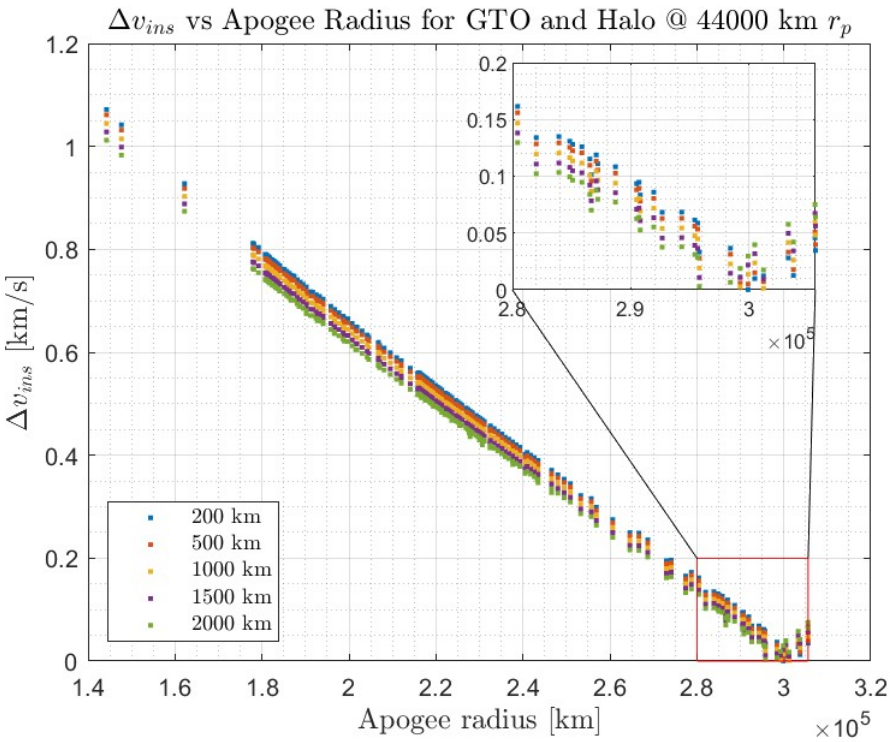

(a) Δv_{INS} cost.

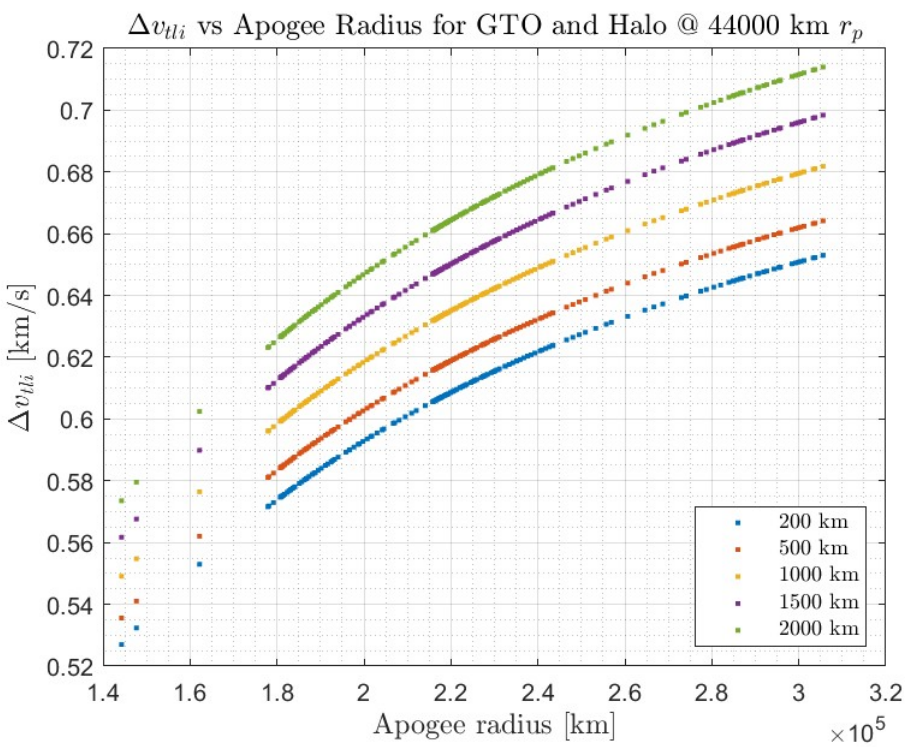

(b) Δv_{TLI} cost.

Figure 4.4: Δv cost for the individual burns with GTO as parking orbit.

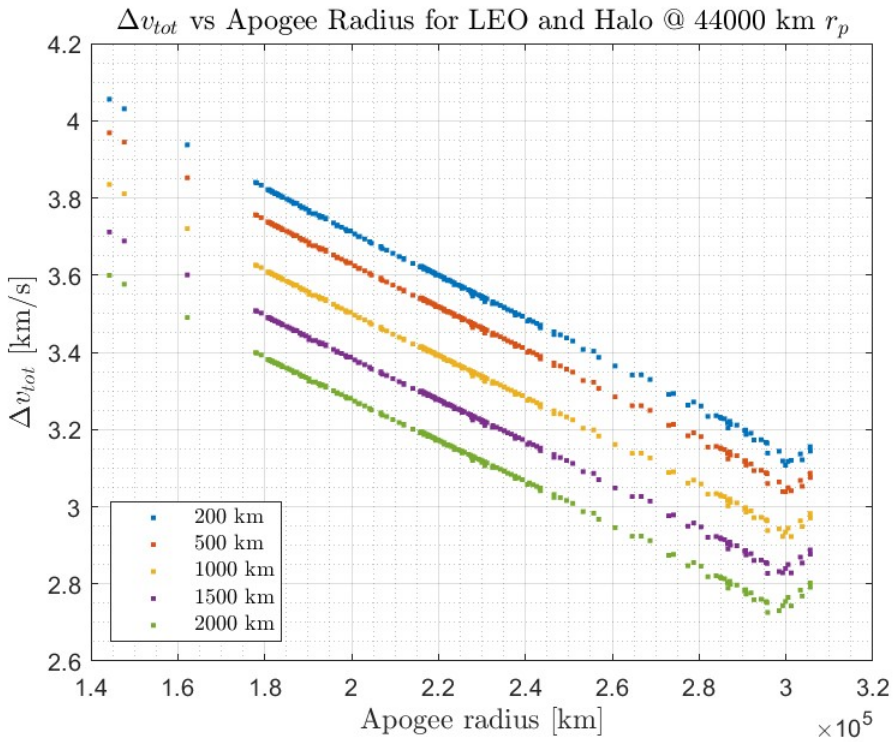

(a) $r_p = 44000$ km.

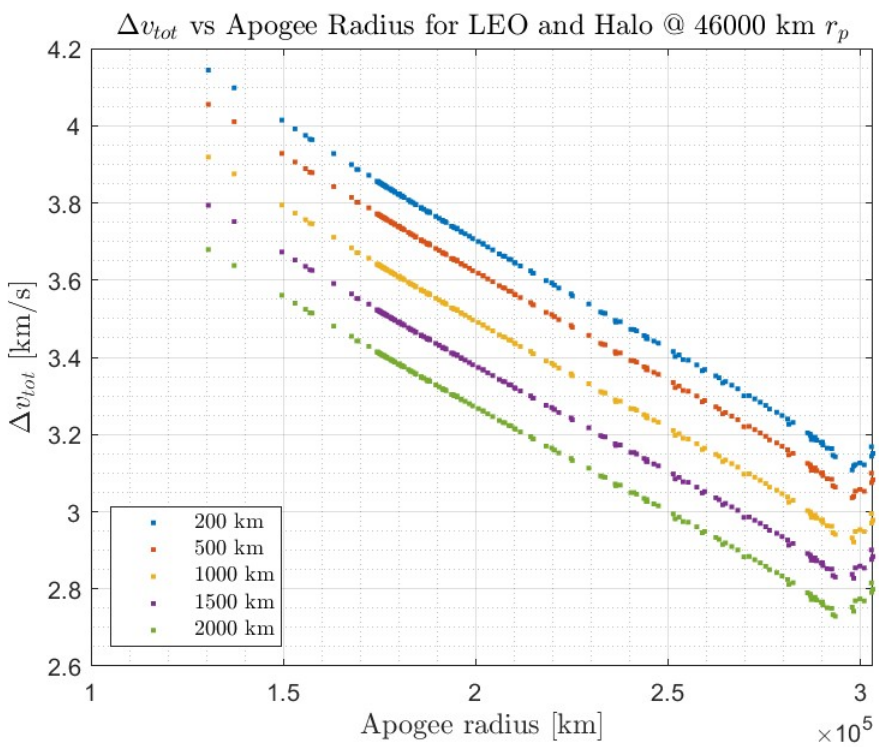

(b) $r_p = 46000$ km.

Figure 4.5: Total Δv cost for different Halo with LEO as parking orbit

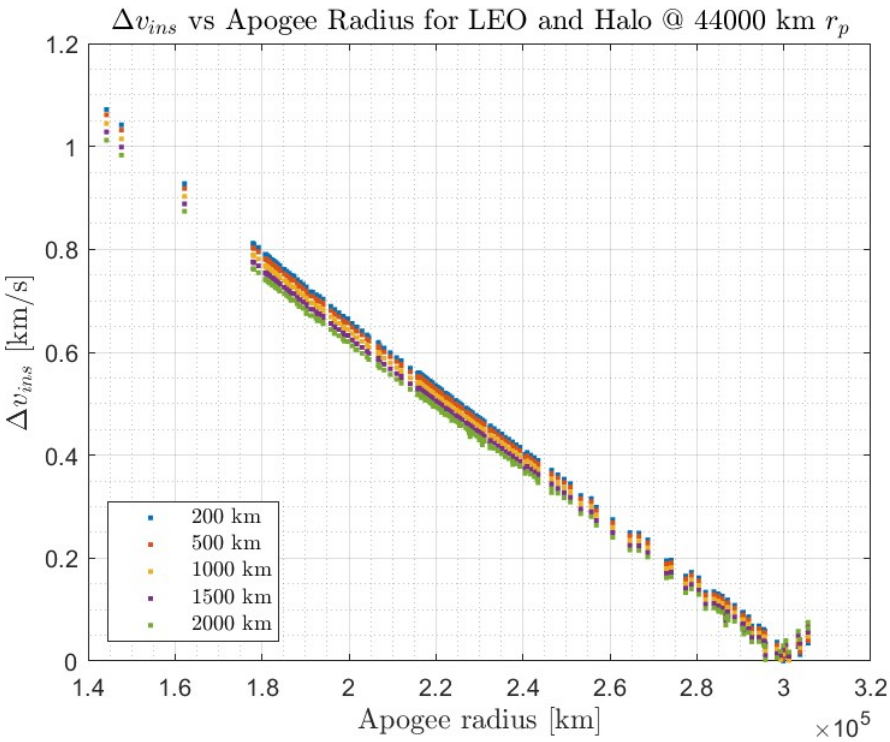

(a) Δv_{INS} cost.

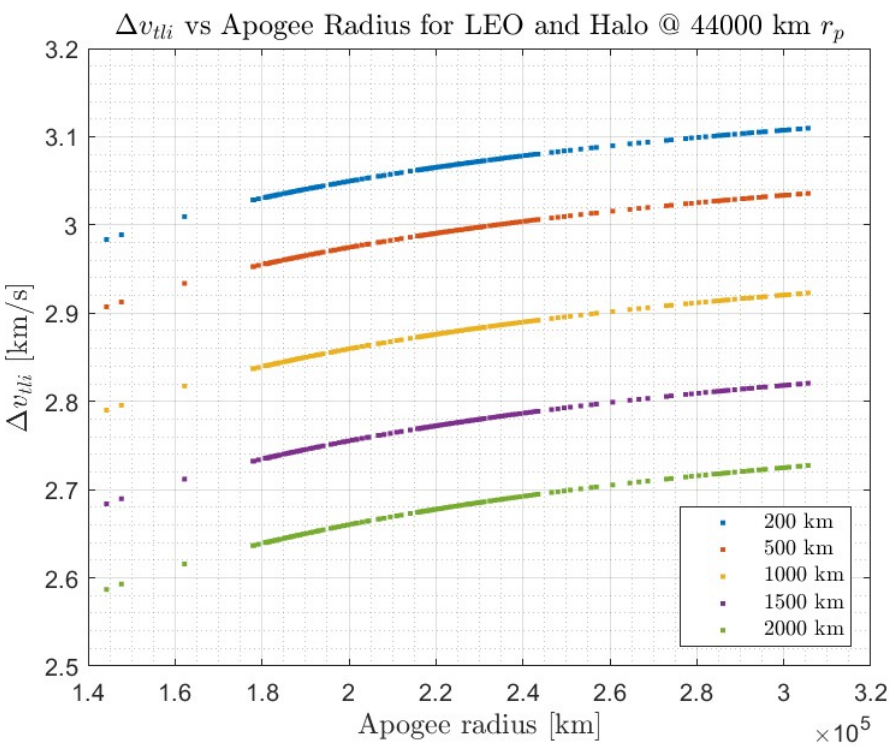

(b) Δv_{TLI} cost.

Figure 4.6: Δv cost for the individual burns with LEO as parking orbit.

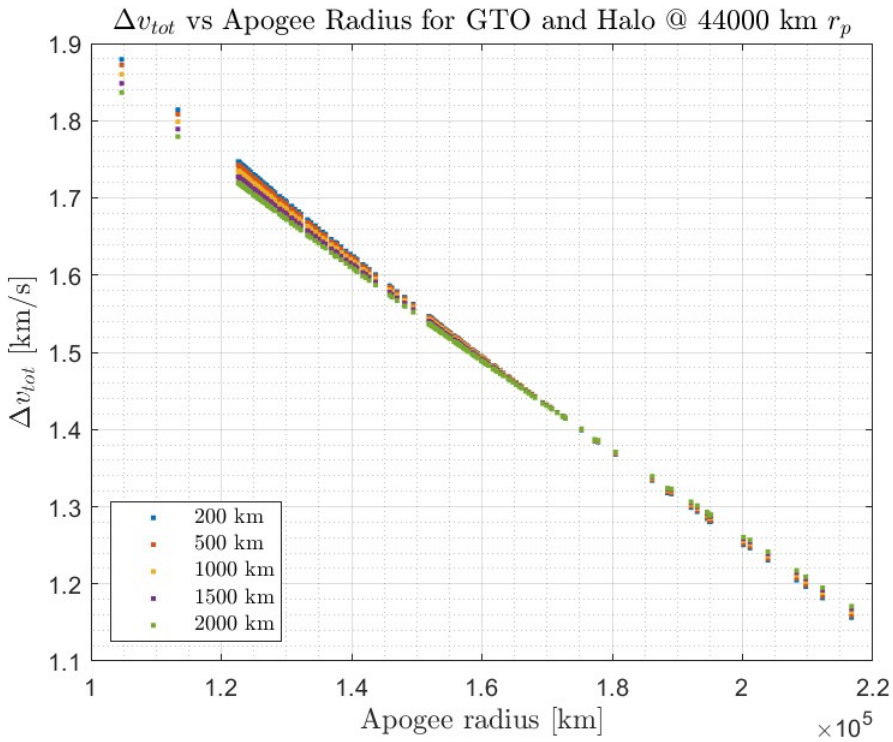

(a) $r_p = 44000$ km .

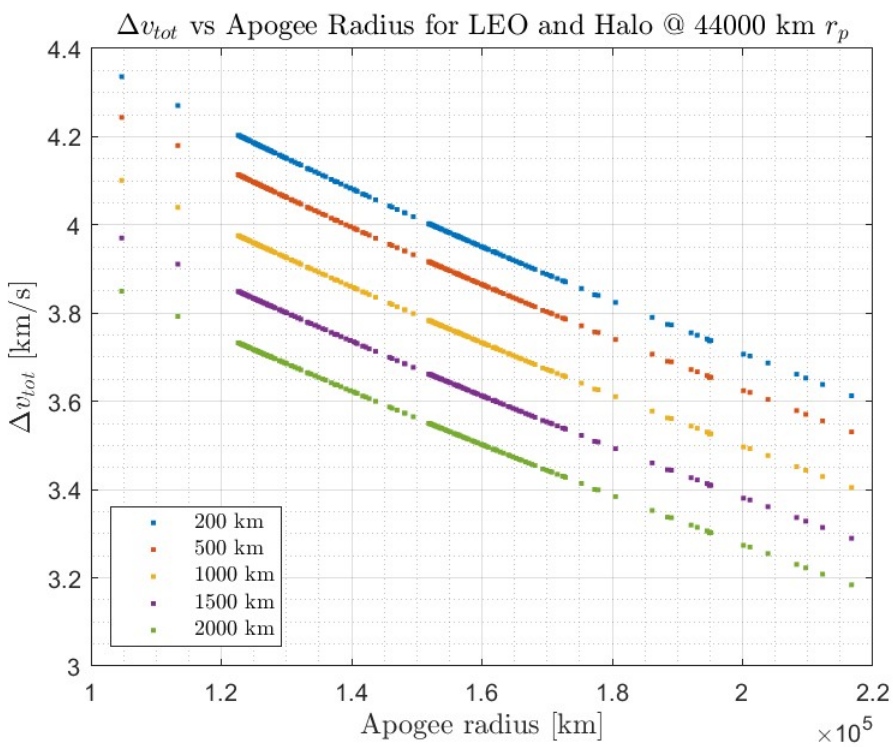

(b) $r_p = 46000$ km.

Figure 4.7: Total Δv cost for LEO and GTO for Poincaré section B.

For each parking orbit type the minimum possible Δv is selected and presented in Figures 4.8 and 4.9. Figure 4.8 suggests that a lower perigee altitude is desired for a GTO orbit with the lowest options spread around 0.65 to 0.66 km/s. For the LEO case, the behavior is quite different suggesting that a higher orbital radius is more feasible with maneuver cost ranging from nearly 3.1 to 2.71 km/s as perigee increases. Regarding the behavior with respect to Halo orbit selection, it is observed that the higher perilune orbits are cheaper to travel for both cases. As the results suggest, a transfer from LEO is more demanding, hence, a GTO with a perigee altitude of 200 km is selected as a parking orbit for further analysis.

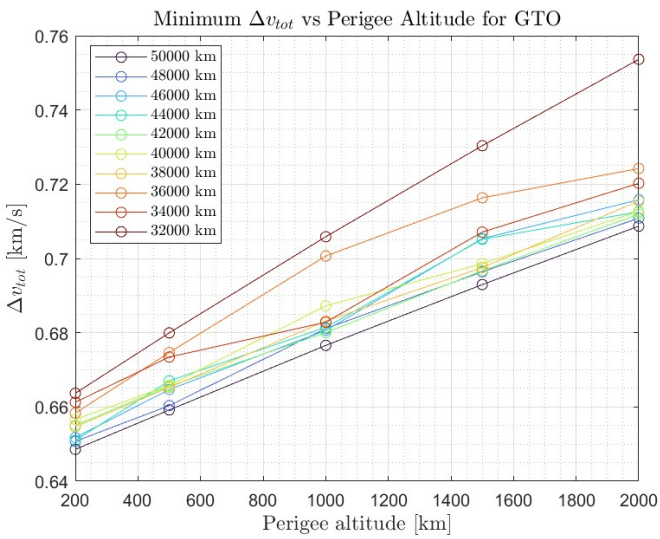

Figure 4.8: Minimum Δv cost GTO.

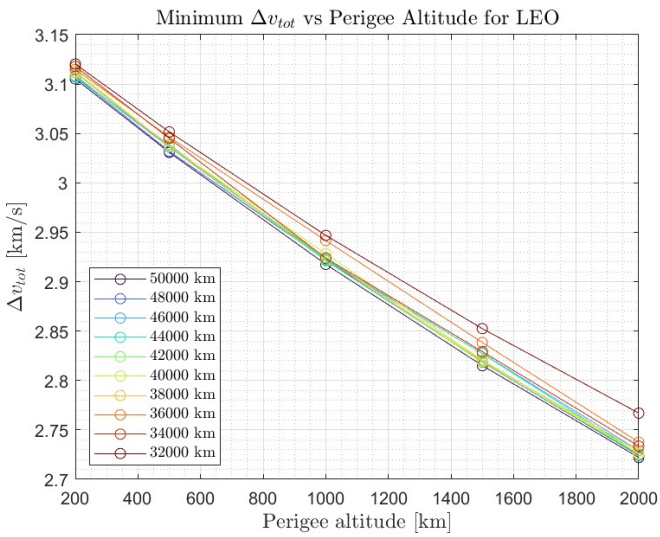

Figure 4.9: Minimum Δv cost LEO.

4.3.2. Targeting and optimizing in CRTBP

Although the Hohmann approach is sufficient to visualize the behavior of the transfer options, a refined solution is required to obtain a higher fidelity result since the insertion altitude is very high and the effect of the dynamics of the CRTBP is significant. The refinement is conducted by applying a targeting algorithm and optimizing the results by minimizing the cost function. The cost function for the problem is defined as,

$$J = \Delta v_{TLI} + \Delta v_{INS}, \tag{4.10}$$

Hence minimizing the cost function results in a minimized maneuver cost. The algorithm works in two main steps: the generation of an initial guess and optimization of the Δv_{TOT}. Here it is important to note that, for all the steps the propagation occurs backward in time. First of all, a generic targeting algorithm is applied that targets a spherical region around the Earth thus ensuring that the initial guess reaches a feasible distance to Earth. The targeted state defined as,

$$R_{sphere} = R_e + h, \tag{4.11}$$

where R_{des} is the radius of the sphere, R_e is the radius of the Earth and h is the desired Earth altitude. The radius of the sphere can be selected arbitrarily, the aim of this first targeter is just to ensure that the initial guess is close to Earth. In this study, it is selected as 200 km. To start the targeting algorithm again an initial guess is required. It is provided by the results based on the Hohmann approach. The insertion maneuver corresponding to the minimum cost solution is applied parallel to the velocity at the edge of the manifold. Then the braking maneuver is varied on all three axes with the time of flight until the desired objective is obtained.

As the second step, the initial guess is fed into an optimizer such that Equation (4.10) is minimized. In the optimizer, the trajectory is propagated backward up to a close region around Earth then an impulsive maneuver is applied parallel to the approach velocity while targeting a desired eccentricity. In this step, four constraints are applied. The first one is similar to initial guess generation such that at the end of the flight between the stable manifold insertion point and parking injection point, the distance between the satellite and the Earth is equal to the desired perigee of the orbit. Expression for this constraint is presented as,

$$r_{p,\ park} = r(t_f), \tag{4.12}$$

The second constraint applied is to ensure that the velocity and position vector at time $t = t_f$ is perpendicular to each other so that the second burn is applied at the perigee of the parking orbit. The constraint is defined as,

$$\bar{r}_f \cdot \bar{v}_f = 0, \tag{4.13}$$

As stated before in this analysis the orientation of the parking orbit is not constrained hence an injection from a perfectly aligned perigee is assumed. So the third constraint ensures that the injection maneuver is parallel to the incoming velocity vector, by defining the unit vector of the incoming velocity vector in the inertial frame. Finally, the last constraint is implemented to achieve the eccentricity of the desired parking orbit.

The resulting transfer to a Halo with 40000 km perilune is illustrated in Figure 4.10 in the inertial and rotating frame. Here W_H is the Halo, $W_{H,S}$ is Halo stable manifold trajectory, $W_{S,P}$ is the park transfer trajectory, and W_P is the parking orbit. The total transfer includes a translunar injection of 0.653 km/s, manifold insertion of 0.731 km/s, and total maneuver of 1.384 km/s with a time of flight of 33.7 days for the manifold part and 3.9 days for manifold insertion with a total 37.6 days of transfer duration. Additionally, as seen in Figure 4.10b, the transfer from $W_{H,S}$ and $W_{S,P}$ indicates a costly insertion maneuver burn. This occurs since the algorithm is based on a Hohmann maneuver approximation. A further improvement here could be to design $W_{S,P}$ with a longer time of flight with multiple revolutions around the Earth such as conducting multiple injection maneuvers at the perigee with smaller burns.

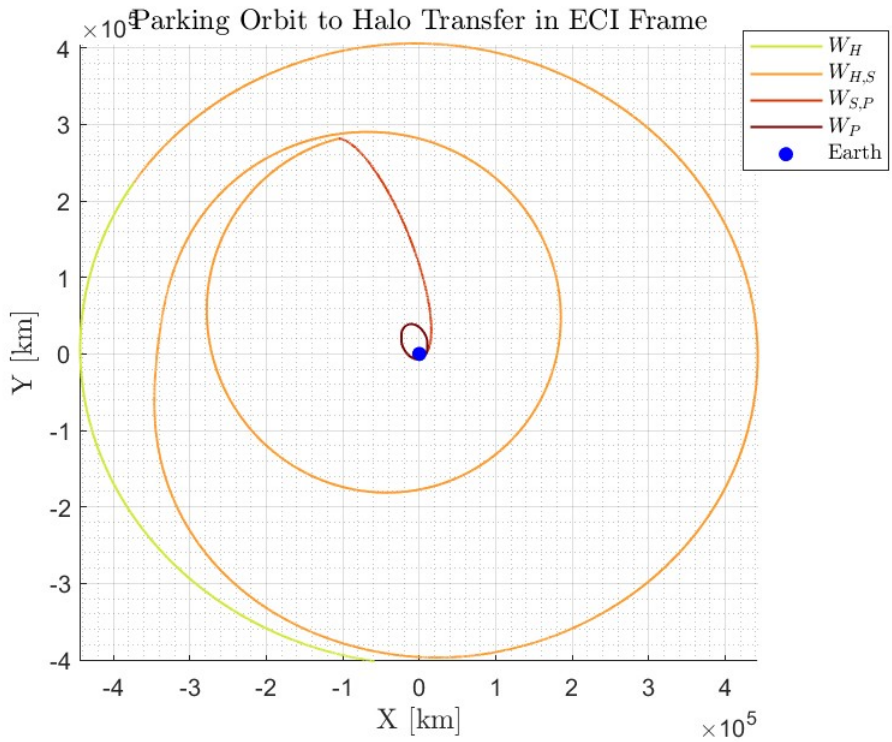

(a) Earth inertial frame.

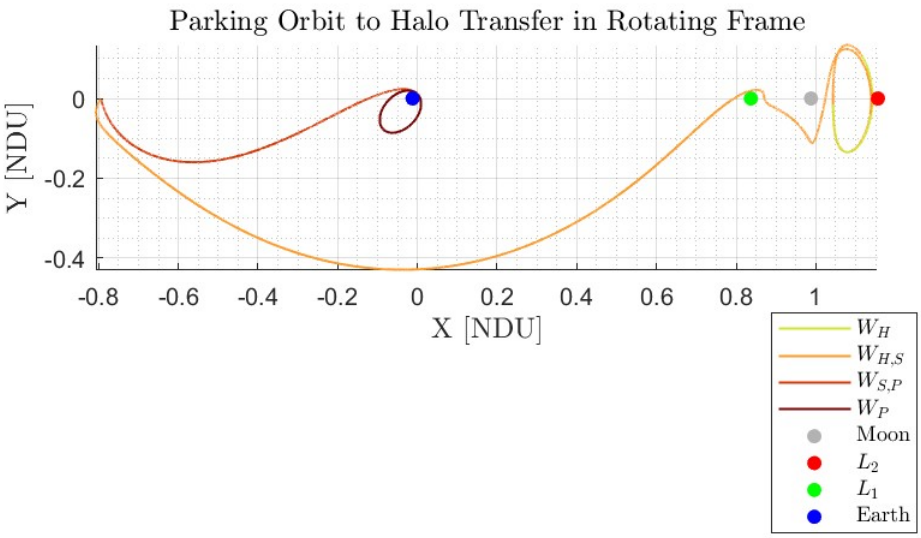

(b) Rotating frame.

Figure 4.10: Transfer to Halo with 40000 km perilune with GTO as parking orbit.

The complete results of the refinement are presented in Table 4.1. It is observed that the insertion maneuvers are much higher compared to the Hohmann approximation. Here the insertion maneuvers are approximately 750 m/s for each orbit. The difference is due to inclination change during the manifold insertion whereas, in the Hohmann-like procedure, every segment is assumed to be perfectly aligned. In contrast, the injection costs are on a similar level with a mean of around 652 m/s indicating that a Hohmann analysis is a good approximation for the initial burn. Furthermore, it is clearly seen that the lower perilune orbits require higher burns to target the manifold insertion point with a minimum value of 0.649 m/s for a 48000 km perilune Halo.

$r_{p,\ Halo}$ $[km]$	Δv_{TLI} $[km/s]$	Δv_{INS} $[km/s]$	Δv_{TOT} $[km/s]$	$ToF_{S,P}$ $[days]$	$ToF_{H,S}$ $[days]$	ToF_{TOT} $[days]$
32000	0.656	0.740	1.396	3.8	58.7	62.5
34000	0.654	0.777	1.431	3.5	79.6	83.0
36000	0.654	0.732	1.386	3.4	43.4	46.7
38000	0.654	0.734	1.388	3.6	36.4	40.0
40000	0.653	0.731	1.384	3.9	33.7	37.6
42000	0.652	0.802	1.454	3.2	70.0	73.2
44000	0.651	0.733	1.384	3.8	31.9	35.7
46000	0.650	0.738	1.388	3.8	31.5	35.3
48000	0.649	0.745	1.394	3.7	33.7	37.4

Table 4.1: Refined results for the parking orbit to Halo transfer.

5 | Halo to NRHO Transfer Design

In this chapter, the methodology to design a transfer trajectory between a Halo and an NRHO is explained in detail. The connections between the periodic orbits corresponding to the same Lagrange points are proven for instance in [6] and [18]. Here the aim is to utilize these connections to construct the transfer trajectory. The overall trajectory consists of three segments: unstable Halo manifold, bridge trajectory, and NRHO stable manifold. The maneuver consists of two burns at the start and the end of the bridge trajectory. Virtually no Δv is required for the injection or ejection from a periodic orbit into manifolds. Similar to the methodology explained in Chapter 4, 500 points along the periodic orbits were selected for the computation of the manifolds for both NRHO and Halo with a maximum time of flight of 1 year. The method conducted here is based on the algorithm explained in the study in [8] where $EM - L_1$ homoclinic connections are deeply analyzed along with some examples for $EM - L_2$. Furthermore with the same method [16] proposed transfers between $EM - L_2$ NRHOs and Halos with maneuvers as low as 50 m/s. Alternatively, to the applied algorithm in this thesis, Poincaré maps could be utilized also in order to see the close passing options for unstable-stable manifold pairs. The alternative application is studied in [8], [13], and [12].

5.1. Sphere of influence

As explained earlier, it is important to establish a good framework where to look for the connection between the hyperbolic manifolds of halo and NRHO associated with L2. This region is based on the sphere of influence of the second primary in this study. In a three-body system, the third body is under the mutual attraction of the remaining bodies at every point. However, due to the inverse square behavior of the gravitational attraction law, the attractive force from a celestial body drops rapidly with increasing distance. This results in a region where the force acting on the satellite is dominated by a single body. The region is defined as the sphere of influence of the related object. Within this region, two-body dynamics are considered to be applicable as a simplification for three-body dynamics. Formulation defined as in Equation (5.1),

$$\frac{r_{SOI}}{R_1} = \left(\frac{m_1}{m_2}\right)^{\frac{2}{5}} \tag{5.1}$$

where r_{SOI} is the radius of the sphere of influence, r_m distance between primaries, m_1 is the mass of the smaller planet and m_2 is the mass of the heavier object. The derivation of Equation (5.1) can be found in [7]. In the Earth-Moon environment, we are mainly interested in the sphere of influence of the Moon, and the related data is presented in Table 5.1,

m_e	m_m	$r_{SOI,m}$
$[kg]$	$[kg]$	$[km]$
5.974×10^{24}	7.348×10^{2}	6.618×10^{4}

Table 5.1: SOI parameters for Earth-Moon system

Here m_e is the mass of the Earth, m_m is the mass of the Moon, and $r_{SOI,m}$ is the radius of the sphere of influence of the Moon.

5.2. Defining bounding sphere

The bounding sphere is defined as the region where the transfer between the stable manifold of the NRHO and the unstable manifold of the halo orbit can take place around the Moon. As explained in [8], the radius of the bounding sphere is selected such that the two-body dynamics is sufficient within the region. In this study, the radius is selected as one-third of r_{SOI}. In Figure 5.1, part of the trajectories within the bounding sphere is shown.

The manifolds are propagated until the trajectory pierces the bounding sphere and the states at that specific point are collected. Here it is important to point out that the manifolds enter the interior of the bounding sphere multiple times hence there may be multiple piercing points for a single trajectory. As seen in Figure 5.1, manifolds pass close to Moon.

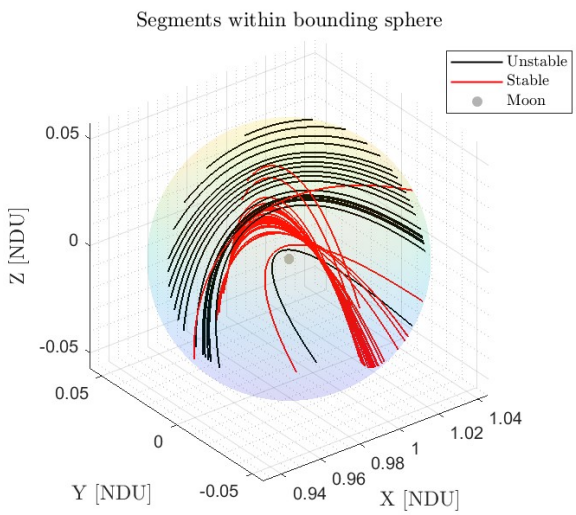

Figure 5.1: Manifolds within the bounding sphere.

Additionally, if an initial condition of the manifold is within the bounding sphere extra caution needs to be taken in order to select the correct piercing point as an outward piercing state would result in incorrect results. In this study, if the manifold starts within the bounding sphere, the first state at the manifold is taken as the inward piercing point.

5.3. Searching for optimal connection points

5.3.1. Defining two-body parameters

As explained earlier, the orbital elements that can be associated with the hyperbolic manifolds at a suitable location can be used to select the best points to select the most optimal points along the manifolds. The aim is to obtain a set of unstable and stable manifolds with minimal shape and orientation differences. Here all these parameters are computed with respect to the smaller primary and in dimensional form. The eccentricity, as defined in Equation (5.2), vector shall be used to define the shape of the orbit.

$$\bar{e} = \frac{\bar{v} \times (\bar{r} \times \bar{v})}{\mu_2} - \frac{\bar{r}}{|\bar{r}|}, \tag{5.2}$$

To define the orientation in space, the normalized angular momentum is defined as,

$$\bar{h}_{norm} = \frac{\bar{h}}{a\mu_2}, \tag{5.3}$$

Here, $\bar{h}$ is the angular momentum vector and a is the semi-major axis defined as,

$$a = \frac{h^2}{\mu_2(1-e^2)}, \tag{5.4}$$

In order to compare the states, the norm of the vectorial differences shall be taken as,

$$\begin{cases} \Delta e = |\bar{e}_u - \bar{e}_s|, \\ \Delta h_{norm} = |\bar{h}_{norm,u} - \bar{h}_{norm,s}|, \end{cases} \tag{5.5}$$

Here the subscripts u and s designate the unstable and stable manifolds. Finally, a scalar value is introduced to combine the two parameters given as,

$$k = \Delta e + \Delta h_{norm}, \tag{5.6}$$

As demonstrated in [8] for multiple Halo orbit connections within Earth-Moon and Earth-Sun environment, the Δv distribution shows an almost linear dependency with parameter k hence searching for the smallest k is optimal to find the cheapest bridge trajectory.

5.3.2. Selection of manifold pair

First, it is necessary to narrow the search area for the optimal connection points since as explained before there may be multiple trajectory segments for the same manifold within the bounding sphere. Hence, the k value of every possible match between different states at the boundary sphere shall be computed in order to select the most feasible pair of trajectories while reducing the computational time. The process is visualized in Figure 5.2. Based on Figure 5.1, the piercing points are filtered thus producing Figure 5.2a. Then after the k value comparison, the optimal pair of unstable-stable manifold is obtained as in Figure 5.2b.

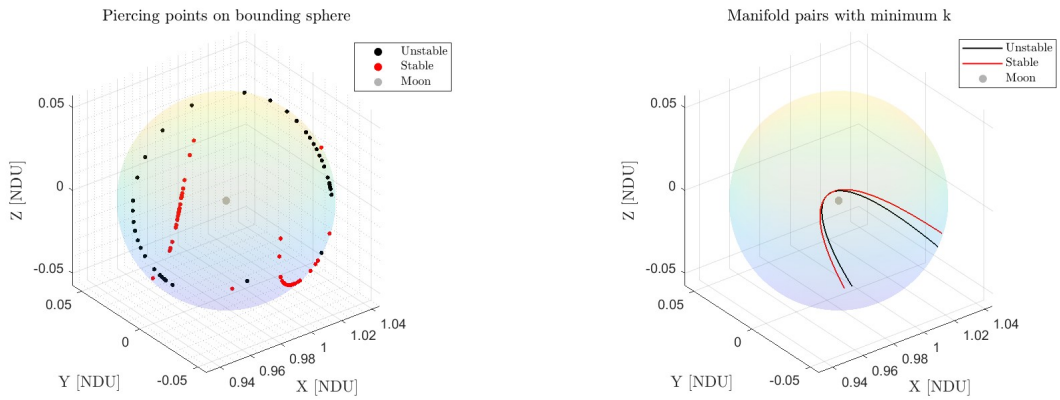

(a) Piercing points. (b) Optimal selection.

Figure 5.2: Process for optimal manifold pair selection.

5.3.3. Selection of connection states

In this step, every possible pair of states within the selected manifold pair shall be checked regarding shape and orientation. Here as suggested in [8], it is possible to reduce the number of possible connection points to save computational time and have a more even distribution of the analyzed points. However, in this study, for the sake of completeness, in this study every possible option along the manifold shall be studied.

5.4. Transfer design between two manifolds

Having selected the states to connect, now a two-burn maneuver strategy shall be conducted to construct the bridge trajectory. The first maneuver Δv_1 occurs at the unstable manifold of the given halo to reach the stable manifold of the given NRHO after a time Δt. A second maneuver follows to insert into the NRHO from the associated stable manifold. A simple shooting algorithm is utilized to compute the whole transfer. Then the result is optimized to achieve the cheapest option. The optimal connection points are selected with a two-body approximation however it is crucial to optimize the trajectory based on the three-body dynamics. As a result, the points are allowed to be adjusted by the optimizer. The optimization problem includes free variables defined as,

$$\alpha = [\Delta t_1 \ \Delta t_2 \ \Delta t_3 \ \Delta v_1 \ \Delta v_2], \tag{5.7}$$

Here, Δt_1 and Δt_2 are the adjustment time of the first and second connection points, Δt_3 is the bridge trajectory time of flight, Δv_1 and Δv_2 are the initial and final burns. There

are no constraints regarding any Δt or Δv. Since the aim is to find the cheapest transfer options, the cost function is defined as in,

$$J = \Delta v_1 + \Delta v_2, \tag{5.8}$$

The scheme of the optimizer problem is illustrated in Figure 5.3 where the blue line represents the incoming stable manifold trajectory, the red dashed line is the bridge trajectory and the green line is the outgoing unstable manifold trajectory.

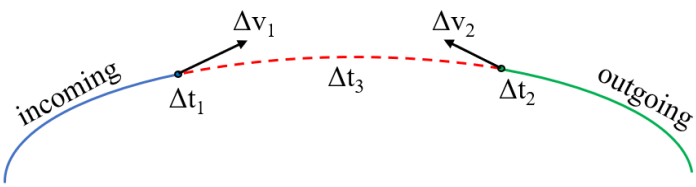

Figure 5.3: Scheme of the optimizer problem.

For the analysis, the Halo orbits from 32000 to 48000 km perilune have been included while the NRHOs from 2000 to 12000 km perilune selected with increments of 2000 km for both periodic orbits. The result of the analysis is presented in Figure 5.4 and 5.5, showing the distribution of total maneuver cost with respect to the Jacobi constant difference between Halo and NRHO pair. Here, the colormap represents the perilune radius of the Halo orbit. The possible maneuvers range between 31 and 200 m/s with the cheapest option between Halo with 40000 km perilune and NRHO with 6000 km perilune. It is clearly observed that the periodic orbit pairs with smaller Jacobi constant differences require cheaper maneuvers for the transfer suggesting that Figure 3.4a provides a good initial guess to search for the optimal selection. As the color distribution indicates, the Halos closer to the Moon are the cheapest options.

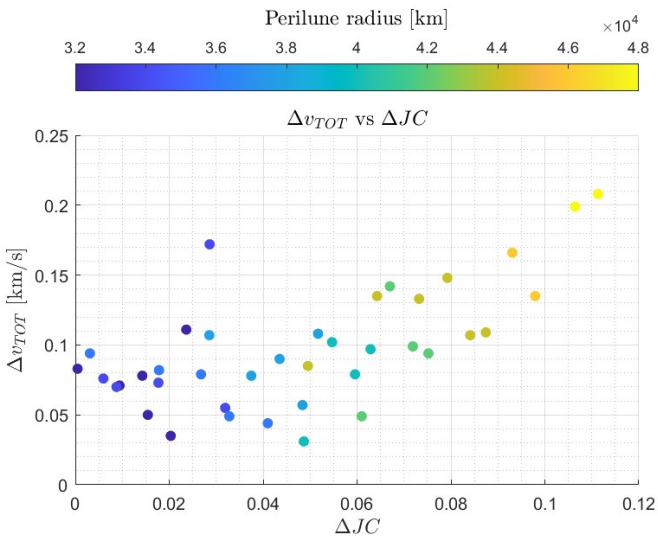

Figure 5.4: Δv_{TOT} distribution with respect to Jacobi constant difference for Halo and NRHO options.

The amount of Δv for each burn is illustrated in Figure 5.5 showing a similar distribution as Δv_{TOT} ranging between 10 and 131 m/s for Δv_{UB} and between 3 and 154 m/s for Δv_{BS}, where Δv_{UB} is the bridge trajectory insertion maneuver and Δv_{BS} is the stable manifold insertion maneuver.

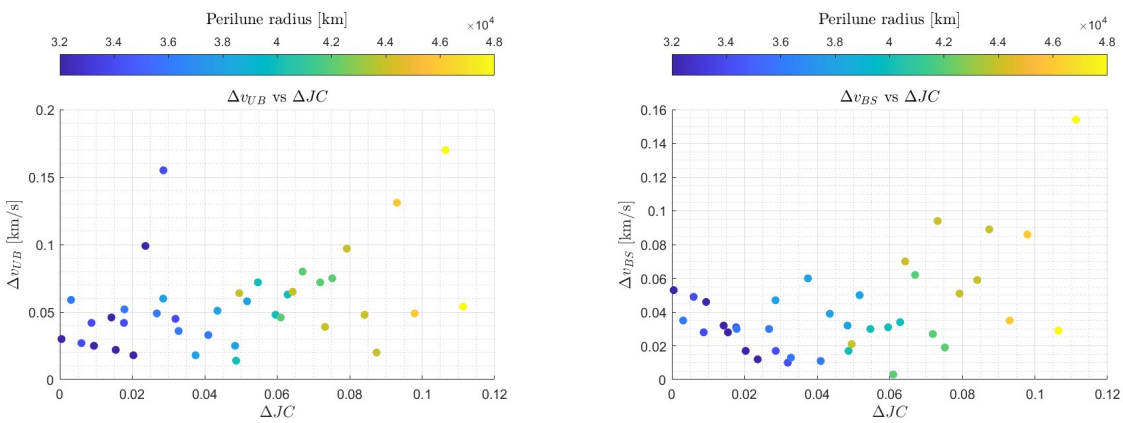

(a) Δv_{UB}. (b) Δv_{BS}.

Figure 5.5: Δv_{UB} and Δv_{BS} distribution with respect to Jacobi constant difference for Halo and NRHO options.

The cheapest transfer trajectory has been presented in Figure 5.6, resulting in a total maneuver cost of 31 m/s and a time of flight of 137 days. Here W_O is the NRHO, $W_{O,S}$

is NRHO stable manifold trajectory, $W_{S,U}$ is the bridge trajectory, $W_{U,H}$ is the unstable Halo trajectory and W_H is the Halo orbit.

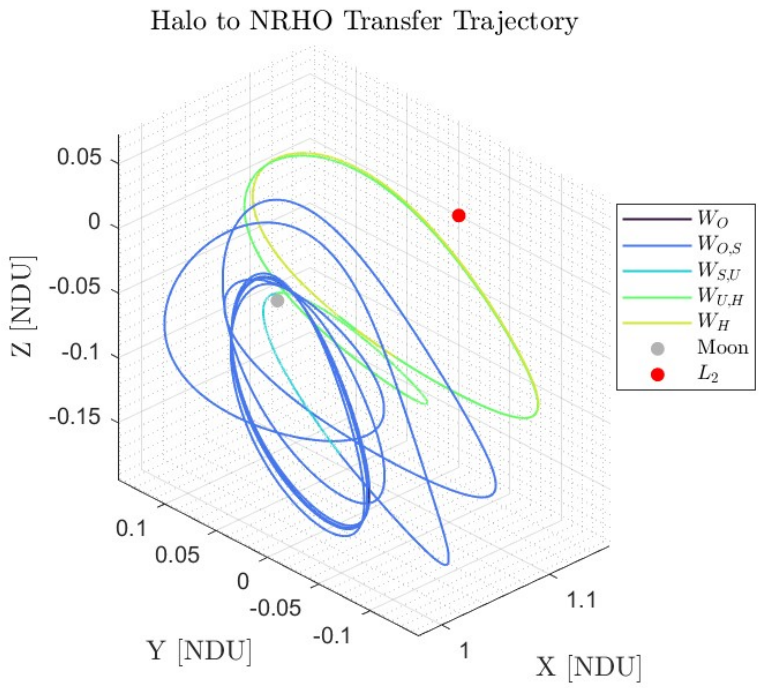

Figure 5.6: Transfer between 40000 km and 6000 km perilune.

During the analysis, it is observed that the fixed-time targeter performs poorly compared to the variable-time targeter in some cases of close Moon flybys. As a result, the bridge trajectory is computed by utilizing a variable-time differential corrector. The dynamical model is a chaotic one so, the resulting Δv solutions are extremely dependent on the number of trajectories to be analyzed and the combination of the selected Halo and NRHO. With the explained methodology, some NRHO and Halo pairs fail to produce sufficient transfer arcs. During the simulation, we have encountered cases where the STM was singular. This happens when the bridge segment approaches very closely the Moon. These results are omitted in this thesis. Possible solutions for these problems are to include bridge trajectories with multiple revolutions around the Moon and with better optimizer/targeter design.

6 | Operational Orbit Selection and Complete Trajectory Design

In this chapter, the complete trajectory from the Earth parking orbit to NRHO is obtained by utilizing the results obtained in Chapter 4 and 5.

The overall scheme of the mission is illustrated in Figure 6.1. The spacecraft shall target an insertion point on the stable manifold of a given halo orbit by applying a maneuver Δv_{TLI} at the perigee of the parking orbit. Then at the apogee, a second burn Δv_{INS} is applied to insert the satellite into the targeted stable manifold. It follows a natural transfer towards the selected halo orbit. Virtually no maneuver is required to insert the satellite into the halo orbit from the stable manifold and then insert it into the corresponding unstable manifold. So, in principle, no specific maneuver is defined for Halo and NRHO insertions. After reaching the intermediate Halo the spacecraft shall follow the unstable halo manifold path up to the close proximity to Moon. Then the maneuver Δv_{UB} is applied in order to place the spacecraft into the bridge trajectory targeting the stable manifold of the NRHO. At the insertion point of the stable manifold associated with the given NRHO, the final maneuver Δv_{BS} is applied and the satellite cruises up to the final operational orbit. As a practical application, the complete trajectory design is proposed as a backup option for the REMEC mission [1].

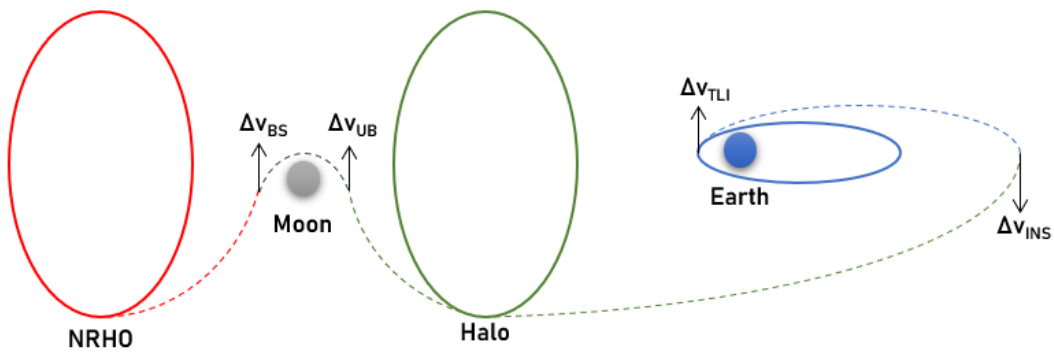

Figure 6.1: Mission scheme.

In order to obtain the complete solution, the trajectory segments between halo and NRHO and halo and parking orbit have to be connected. This is done by implementing a multiple shooting algorithm with predefined patch points along each segment. Here, the trajectory is propagated backward starting from the NRHO orbit.

The multiple shooting algorithm is based on the previously explained variable time differential corrector. In this case, instead of generating one arc, multiple arcs are generated to achieve the complete orbit. The scheme for the multiple-shooting algorithm is presented in Figure 6.2 for four patch points as an example.

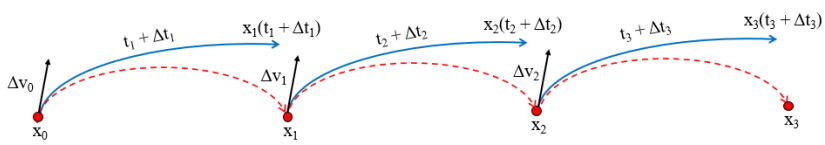

Figure 6.2: Multiple shooting scheme.

First of all, the patch points are defined along with the time of flight between each point. The aim here is to minimize the position errors at the end of the transfer arc. The vector of elements to be minimized for the problem is defined as

$$\Psi = [\Delta x_1 \ \Delta x_2 \ \Delta x_3 \ \Delta x_4 \ \Delta x_5 \ \Delta x_6 \ \Delta x_7]^T, \tag{6.1}$$

The first patch point is defined as a state on the NRHO. The state is propagated for one full period of the NRHO targeting the second state which is the beginning of the stable manifold leading to NRHO. The third point is selected as the state at the beginning of the bridge trajectory followed by the fourth one at the injection into the unstable manifold

of the given halo orbit. Here on, the fifth point is chosen state corresponding to the injection from the unstable manifold to the halo orbit. The sixth patch point corresponds to the injection into the stable manifold of the halo orbit considered. After the trajectory is propagated along the stable manifold, the seventh patch point is defined as the initial state of the transfer arc leading to the parking orbit. The eighth point is the injection into the parking orbit with the ninth state of the parking orbit after one period. Alternatively, the ninth and eighth points are could be taken as the same.

The final results are presented in Table 6.1 and 6.2 for each Halo and NRHO combination. It is observed that the Δv in order to insert or eject from a periodic orbit is of the order of 0.01 m/s so they are excluded from the results. It is clearly seen that the cheapest transfer targets the NRHO of 6000 km with 40000 km Halo as intermediate orbit. The total Δv required is 1.414 km/s resulting in a time of flight of 174.6 days. The operational orbit experiences approximately 69.2 hours of eclipse within a year. The second cheapest transfer targets the NRHO of 12000 km with 36000 km Halo as intermediate orbit. The total Δv required is 1.431 km/s resulting in a time of flight of 281.8 days. The second option experiences approximately 68.5 hours of eclipse within a year.

$r_{p,\ Halo}$ $[km]$	$r_{p,\ NRHO}$ $[km]$	Δv_{TLI} $[km/s]$	Δv_{INS} $[km/s]$	Δv_{UB} $[km/s]$	Δv_{BS} $[km/s]$	Δv_{tot} $[km/s]$	ToF $[days]$	T_{ecl} $[h]$
32000	2000	0.656	0.740	0.046	0.032	1.474	250.4	98.6
32000	4000	0.656	0.740	0.03	0.053	1.480	150.6	73.1
32000	6000	0.656	0.740	0.025	0.046	1.467	172.6	69.2
32000	8000	0.656	0.740	0.022	0.028	1.446	189.3	72.6
32000	10000	0.656	0.740	0.018	0.017	1.441	203.2	71.3
32000	12000	0.656	0.740	0.099	0.012	1.508	264.7	68.5
34000	2000	0.654	0.777	0.027	0.049	1.508	368.6	98.6
34000	4000	0.654	0.777	0.042	0.028	1.501	203.0	73.1
34000	6000	0.654	0.777	0.042	0.031	1.505	189.2	69.2
34000	10000	0.654	0.777	0.155	0.017	1.603	219.6	71.3
34000	12000	0.654	0.777	0.045	0.01	1.487	228.9	68.5
36000	2000	0.654	0.732	0.059	0.035	1.480	346.8	98.6
36000	4000	0.654	0.732	0.052	0.030	1.470	161.5	73.1
36000	6000	0.654	0.732	0.049	0.030	1.466	147.5	69.2
36000	8000	0.654	0.732	0.036	0.013	1.436	180.2	72.6
36000	12000	0.654	0.732	0.033	0.011	1.431	281.8	68.5
38000	4000	0.654	0.734	0.060	0.047	1.496	161.4	73.1
38000	6000	0.654	0.734	0.018	0.060	1.467	175.8	69.2
38000	8000	0.654	0.734	0.051	0.039	1.479	153.2	72.6
38000	10000	0.654	0.734	0.025	0.032	1.445	175.7	71.3
38000	12000	0.654	0.734	0.058	0.050	1.500	246.8	68.5

Table 6.1: Transfer options from Earth to $EM - L_2$ NRHO.

$r_{p,\ Halo}$ $[km]$	$r_{p,\ NRHO}$ $[km]$	Δv_{TLI} $[km/s]$	Δv_{INS} $[km/s]$	Δv_{UB} $[km/s]$	Δv_{BS} $[km/s]$	Δv_{tot} $[km/s]$	ToF $[days]$	T_{ecl} $[h]$
40000	6000	0.653	0.731	0.014	0.017	1.414	174.6	69.2
40000	8000	0.653	0.731	0.072	0.030	1.486	132.6	72.6
40000	10000	0.653	0.731	0.048	0.031	1.463	174.4	71.3
40000	12000	0.653	0.731	0.063	0.034	1.481	245.5	68.5
42000	6000	0.652	0.802	0.046	0.003	1.504	208.4	69.2
42000	8000	0.652	0.802	0.08	0.062	1.596	213.0	72.6
42000	10000	0.652	0.802	0.072	0.027	1.553	210.3	71.3
42000	12000	0.652	0.802	0.075	0.019	1.548	279.3	68.5
44000	2000	0.651	0.733	0.064	0.021	1.470	236.6	98.6
44000	4000	0.651	0.733	0.065	0.070	1.520	295.0	73.1
44000	6000	0.651	0.733	0.039	0.094	1.518	160.7	69.2
44000	8000	0.651	0.733	0.097	0.051	1.533	165.2	72.6
44000	10000	0.651	0.733	0.048	0.059	1.491	162.6	71.3
44000	12000	0.651	0.733	0.020	0.089	1.494	231.4	68.5
46000	8000	0.650	0.738	0.131	0.035	1.555	165.8	72.6
46000	10000	0.650	0.738	0.049	0.086	1.524	163.1	71.3
48000	8000	0.649	0.745	0.17	0.029	1.598	171.0	72.6
48000	10000	0.649	0.745	0.054	0.154	1.603	168.3	71.3

Table 6.2: Additional transfer options from Earth to $EM - L_2$ NRHO.

The trajectories for the two optimal solutions are illustrated in Figure 6.4 and 6.3 in the rotating and inertial frame. Also, the evolution of the distances to the primaries is shown in Figure 6.5 and 6.6 where the negative x-axis is due to the backward propagation. For the first option, the maximum distance to the Earth occurs during the travel along the unstable Halo manifold with a magnitude of 451557 km and the minimum Moon pass takes place at the bridge trajectory with a 2333 km distance. Regarding the second option, the maximum Earth distance is found as 447945 km at the Halo with the minimum Moon distance of 4324 km during the bridge segment.

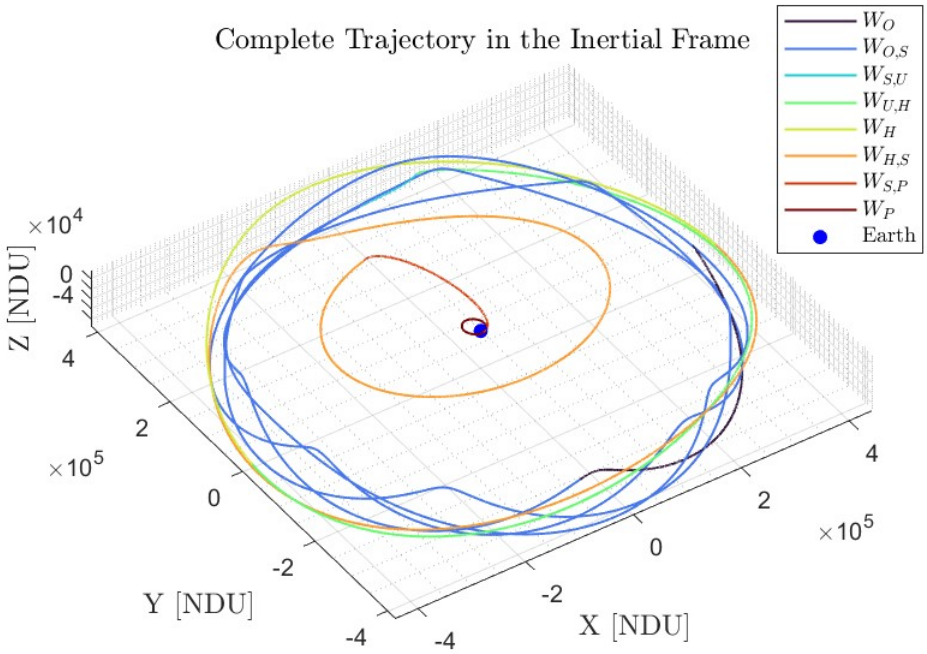

(a) Earth centered inertial frame.

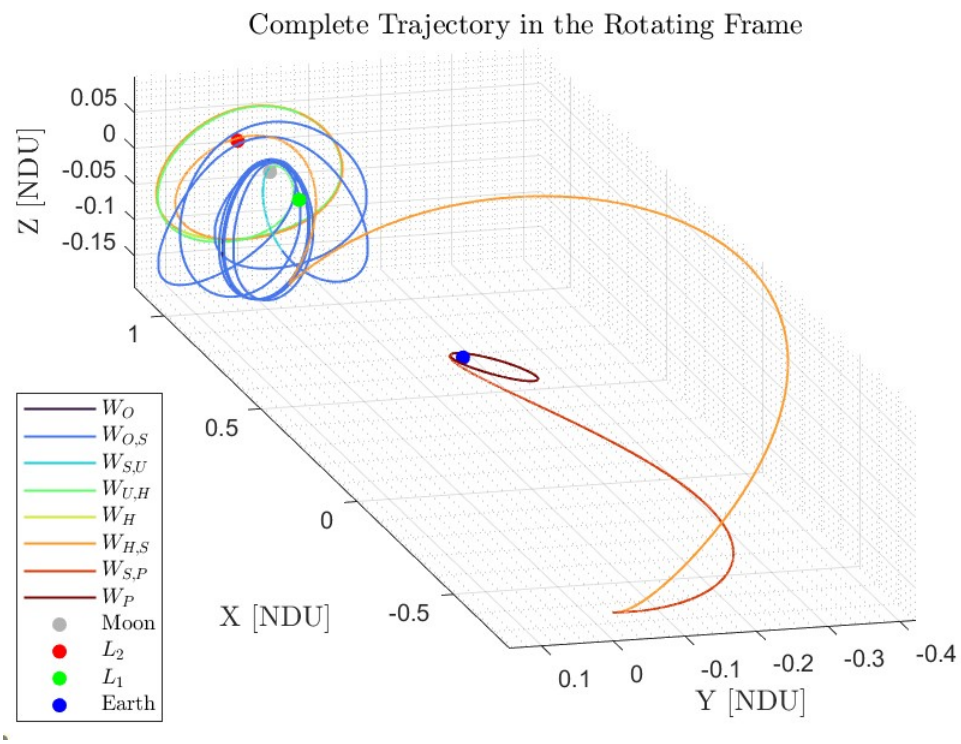

(b) Rotating frame.

Figure 6.3: Transfer to a NRHO with 6000 km perilune and intermediate Halo with 40000 km perilune.

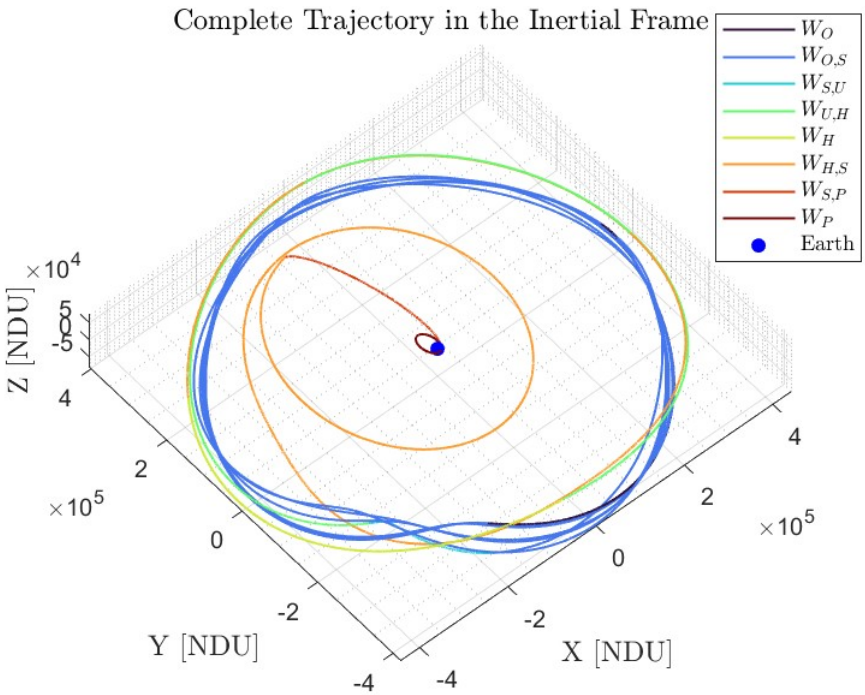

(a) Earth centered inertial frame.

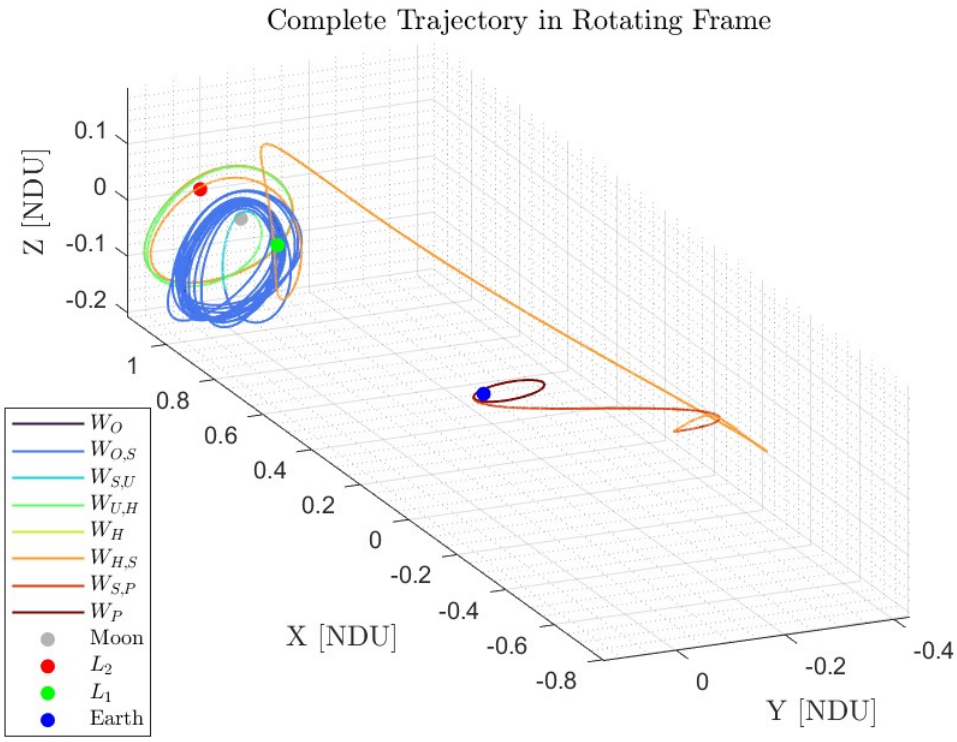

(b) Rotating frame.

Figure 6.4: Transfer to a NRHO with 12000 km perilune and intermediate Halo with 36000 km perilune.

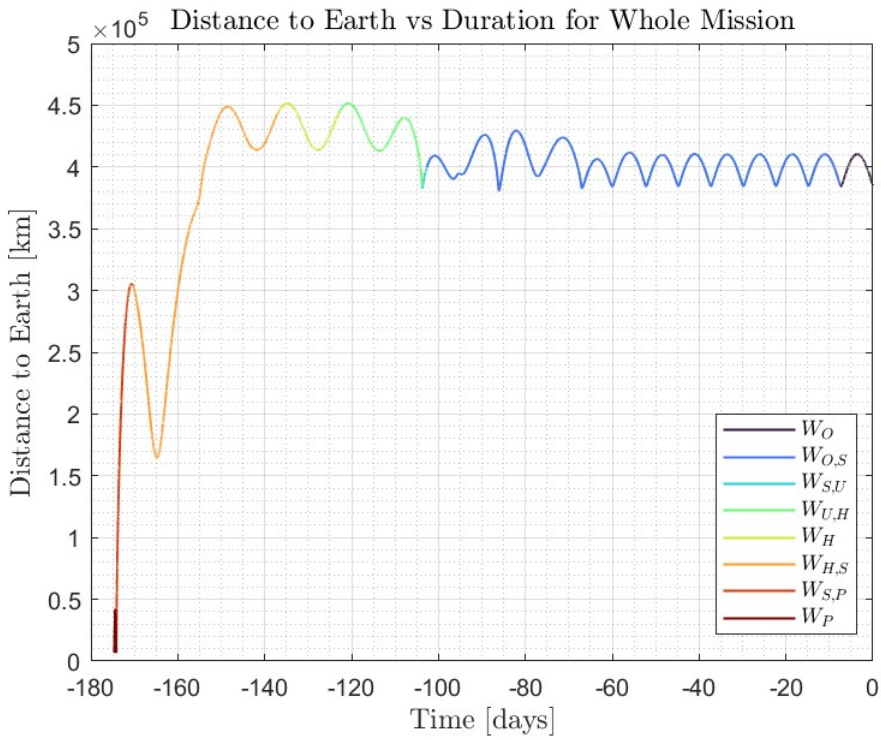

(a) Distance to the Earth.

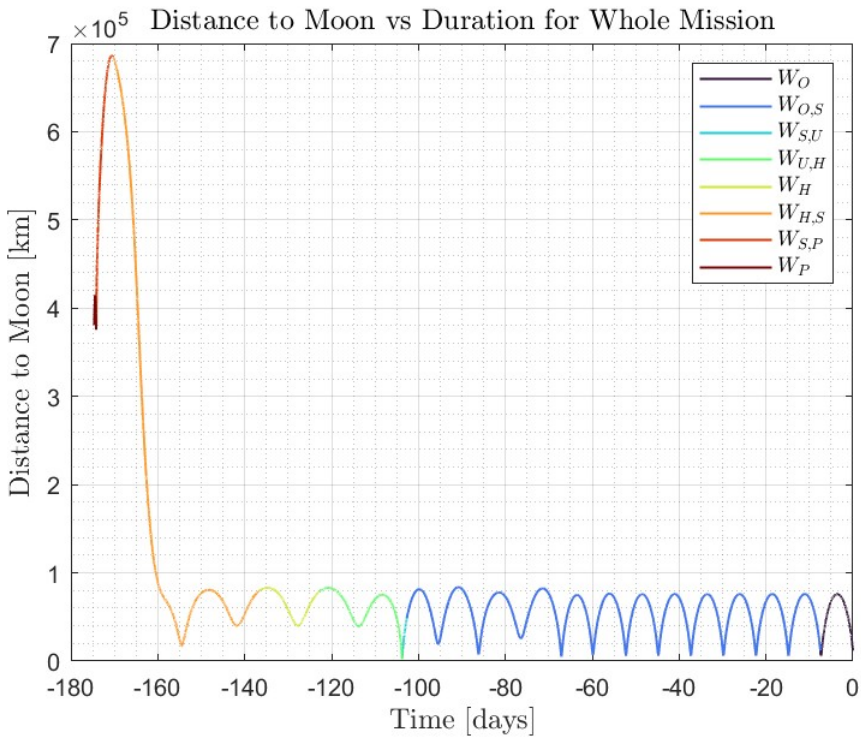

(b) Distance to the Moon.

Figure 6.5: Distance to primaries during transfer for the first option.

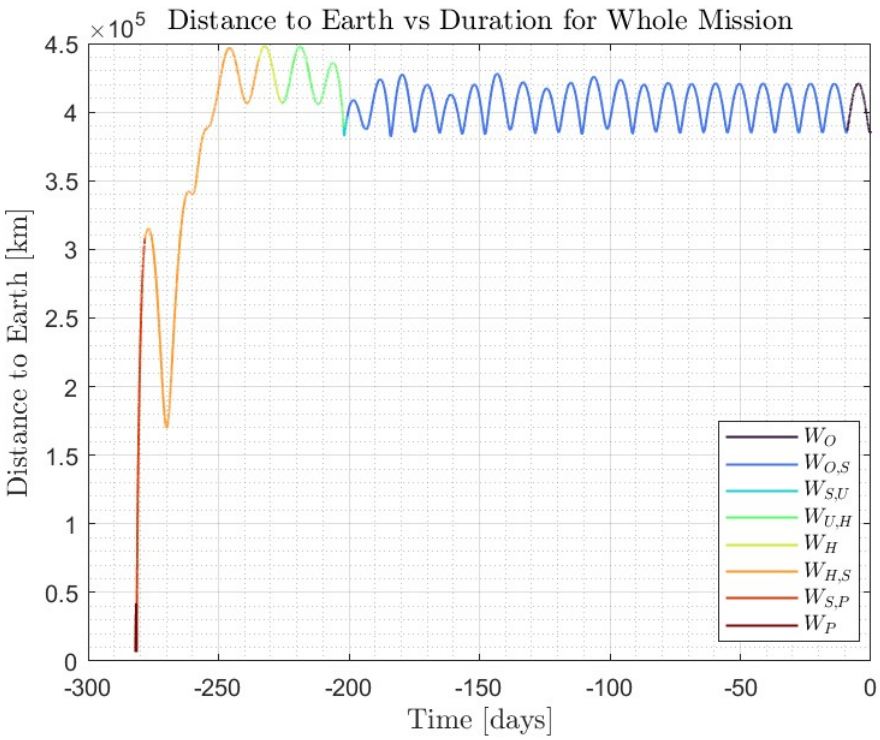

(a) Distance to the Earth.

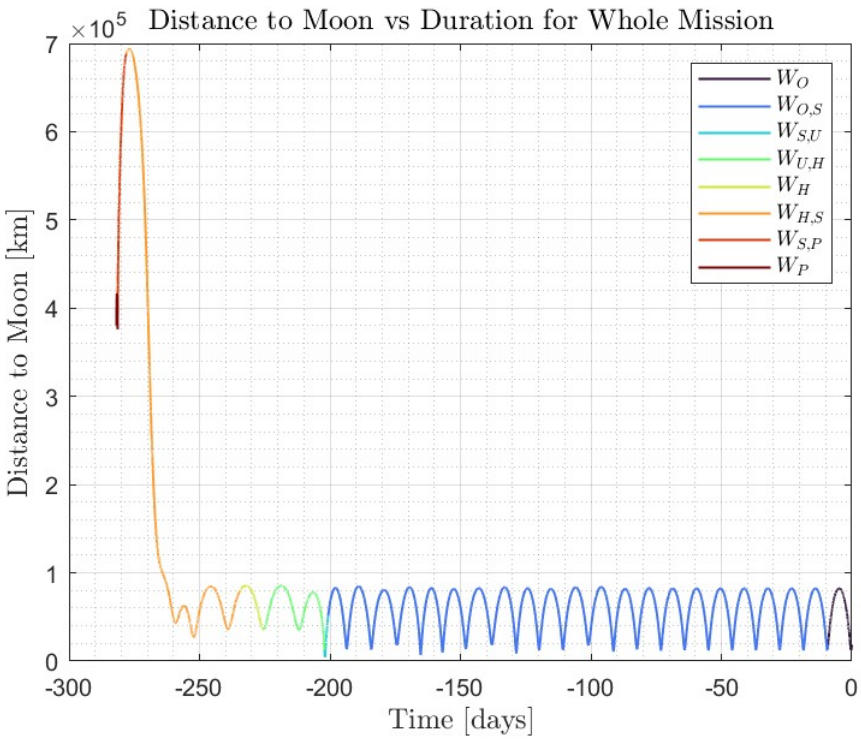

(b) Distance to the Moon.

Figure 6.6: Distance to primaries during transfer for the second option.

7 | Summary and future developments

To summarize, in this thesis, a parametric analysis for the transfer options to $EM - L_2$ by utilising the invariant manifold theory has been studied in detail. The Halo and NRHO families at $EM - L_2$ are generated and their characteristics are discussed. It is clearly shown that the distinction for the NRHO family is the stable behaviour of the periodic orbits compared to the Halo family. Furthermore, an eclipse analysis is conducted for the NRHO family. It is demonstrated that the periodic orbits closer to the Moon experience greater eclipse time within a year with a maximum of 109 hours for a perilune of 2000 km. After 4000 km the overall eclipse duration remains around 70 hours per year. Then a parametric analysis is conducted for the trajectory design from an Earth parking orbit to a halo orbit considering various Poincaré sections, parking orbit types, and parking orbit perigee altitudes. A transfer from GTO would require cheaper maneuvers saving up to 2.0 km/s of Δv compared to a LEO option. Additionally, it is deduced that for a GTO selection a higher perigee results in costlier burns. With the analyzed Poincaré sections type A is shown to be a better option. These results suggest that the cheapest option is to utilise a GTO with a perigee altitude of 200 km with transfers occurring at the type A Poincaré section. This selection corresponds to a total maneuver of 1.384 km/s with a time of flight of 37.6 days to reach the Halo with a 40000 km of perilune radius. Then a parametric analysis between a Halo and NRHO pair is conducted demonstrating the existence of multiple low-cost transfers in the range of 31 - 200 m/s. The most feasible option is a transfer between a NRHO and Halo with 6000 and 40000 km of perilune, respectively with Δv of 31 m/s and a transfer time of 137 days. As the last step, the complete trajectory is obtained by merging the two solutions resulting in a total time of flight of 174.6 days and maneuver of 1.414 km/s.

The transfer between the parking orbit and the stable manifold is based on a Hohmann analysis. As a result, cheaper options could exist that apply a different approach such as increasing the apogee of the transfer arc with multiple burns at perigee or increasing the stable Halo manifold transfer time to search for closer Earth approaches. Additionally for

the NRHO-Halo transfer, searching for a higher number of trajectories along the manifold increases the chance for an even more optimal match so searching for a finer grid in the parametric design could be applied as well. Furthermore, the bridge trajectory design could be augmented to allow multiple rotations around the Moon. In this study, the parking orbit orientation is not a design parameter however in a real application the selection of the operational orbit has to consider the commercial launcher capabilities. So possible orientation correction maneuvers have to be added to total maneuver costs. A detailed solar perturbation analysis is crucial with the proposed time of flight. Moreover, all of these analyses have to be conducted in higher fidelity dynamical models such as the bi-circular four-body problem, elliptical restricted three-body problem, or ephemeris model in order to compute a more realistic transfer scenario.

Bibliography

[1] A. Aguilar, R. Filgas, C. Colombo, E. M. Alessi, M. lo Iacono, E. Arikan, M. Bolis, and et al. The remec mission: Mission concept and architecture feasibility assessment, 04 2023.

[2] E. M. Alessi, G. Gomez, and J. Masdemont. Two-manoeuvres transfers between leos and lissajous orbits in the earth-moon system. *Advances in Space Research*, 45:1276–, 05 2010. doi: 10.1016/j.asr.2009.12.010.

[3] F. Bernelli, Topputo, and F. Massati. Assessment of mission design including utilization of libration points and weak stability boundaries, 2004.

[4] G. Bucchioni, S. Lizy-Destrez, T. Vaujour, V. Thoraval, L. Rouverand, and C. Silva. Phasing with near rectilinear halo orbits: Design and comparison. *Advances in Space Research*, 71(5):2449–2466, 2023. ISSN 0273-1177. doi: https://doi.org/10.1016/j.asr.2022.10.036. URL `https://www.sciencedirect.com/science/article/pii/S0273117722009747`.

[5] E. Canalias, G. Gomez, M. Marcote, and J. Masdemont. Assessment of mission design including utilization of libration points and weak stability boundaries, 2004.

[6] C. C. Conley. Low energy transit orbits in the restricted three-body problems. *Siam Journal on Applied Mathematics*, 16:732–746, 1968.

[7] H. Curtis. *Orbital Mechanics for Engineering Students*. Elsevier, 2005.

[8] K. Davis, R. Anderson, D. Scheeres, and G. Born. The use of invariant manifolds for transfers between unstable periodic orbits of different energies. *Celestial Mechanics and Dynamical Astronomy*, 107:471–485, 05 2010. doi: 10.1007/s10569-010-9285-3.

[9] ESA. Orbiting lunar gateway. `https://www.esa.int/ESA_Multimedia/Images/2019/07/Orbiting_lunar_Gateway`. Accessed: 2023-03-21.

[10] R. Farquhar. *The Control and Use of Libration Point Satellites*. PhD thesis, MIT, 1968.

[11] A. Farrés, C. Gao, J. J. Masdemont, G. Gómez, D. C. Folta, and C. Webster. Geometrical analysis of station-keeping strategies about libration point orbits. *Journal of Guidance, Control, and Dynamics*, 45(6):1108–1125, 2022. doi: 10.2514/1.G006014. URL `https://doi.org/10.2514/1.G006014`.

[12] G. Gomez and J. Masdemont. Some zero cost transfers between libration point orbits. 105, 01 2000.

[13] G. Gomez, W. Koon, M. Lo, J. Marsden, and S. Ross. Connecting orbits and invariant manifolds in the spatial three-body problem. *Nonlinearity*, 17:1571, 05 2004. doi: 10.1088/0951-7715/17/5/002.

[14] D. P. Gordon. Transfers to earth-moon l2 halo orbits using lunar proximity and invariant manifolds. Master's thesis, Purdue University, 2008.

[15] D. J. Grebow. Generating periodic orbits in the circular restricted three-body problem with applications to lunar south pole coverage. Master's thesis, Purdue University, 2006.

[16] C. S. Lara and J. P. S. Cuartielles. Near rectilinear orbits around the moon as operational orbit for the future deep space gateway. 11 2018.

[17] M. Loucks, K. Post, and J. Carrico. Lunar near rectilinear orbits and cis-lunar transfer trajectories in support of the deep space proving ground. *26th AAS/AIAA Space Flight Mechanics Meeting*, 2016.

[18] R. McGehee. *Some homoclinic orbits for the restricted three body problem*. PhD thesis, University of Wisconsin, 1969.

[19] T. Parker and L. Chua. *Practical Numerical Algorithms for Chaotic Systems*. Springer-Verlag., 1989.

[20] T. A. Pavlak. Mission design applications in the earth-moon system: Transfer trajectories and stationkeeping. Master's thesis, Purdue University, 2010.

[21] P. Pergola and E. M. Alessi. Libration point orbit characterization in the earth–moon system. *Monthly Notices of the Royal Astronomical Society*, 426(2):1212–1222, 2012. doi: 10.1111/j.1365-2966.2012.21585.x.

[22] E. Perozzi and A. Salvo. Novel spaceways for reaching the moon: An assessment for exploration. *Celestial Mechanics and Dynamical Astronomy*, 102:207–218, 09 2008. doi: 10.1007/s10569-008-9156-3.

[23] R. R. Rausch. Earth to halo orbit transfer trajectories. Master's thesis, Purdue University, 2005.

[24] M. Shirobokov, S. Trofimov, and M. Ovchinnikov. Survey of station-keeping techniques for libration point orbits. *Journal of Guidance, Control, and Dynamics*, 40 (5):1085–1105, 2017. doi: 10.2514/1.G001850. URL `https://doi.org/10.2514/1.G001850`.

[25] S. Singh, B. Anderson, E. Taheri, and et al. Low-thrust transfers to southern l2 near-rectilinear halo orbits facilitated by invariant manifolds. *Journal of Optimization Theory and Applications*, 191:517–544, 2021. doi: https://doi.org/10.1007/s10957-021-01898-9.

[26] S. Soldini. *Design and Control of Solar Radiation Pressure Assisted Missions in the Sun-Earth Restricted Three-Body Problem*. PhD thesis, University of Southhampton, 06 2016.

[27] S. Strogatz. *Nonlinear Dynamics and Chaos: With Applications to Physics, Biology, Chemistry, and Engineering*. Perseus Books Publishing., 1994.

[28] V. Szebehely. *Theory of Orbits: The Restricted Problem of Three Bodies*. Academic Press Inc., 1967.

[29] D. A. Vallado. *Fundamentals of Astrodynamics and Applications*. The Space Technology Library, 2013.

[30] M. A. Viscio, N. Viola, S. Corpino, S. Stesina, C. Circi, S. Fineschi, and F. Fumenti. Interplanetary cubesats mission to earth-sun libration point for space weather evaluations. volume 2, 01 2013.

[31] R. J. Whitley, D. C. Davis, L. M. Burke, B. P. McCarthy, R. J. Power, M. L. McGuire, and K. C. Howell. Earth-moon near rectilinear halo and butterfly orbits for lunar surface exploration. *28th AAS/AIAA Space Flight Mechanics Meeting*, 2018.

[32] J. Williams, D. Lee, R. Whitley, K. Bokelmann, D. Davis, and C. Berry. Targeting cislunar near rectilinear halo orbits for human space exploration. 02 2017.

[33] R. Zhang, Y. Wang, Y. Shi, C. Zhang, and H. Zhang. Performance analysis of impulsive station-keeping strategies for cis-lunar orbits with the ephemeris model. *Acta Astronautica*, 198:152–160, 2022. ISSN 0094-5765. doi: https://doi.org/10.1016/j.actaastro.2022.05.054. URL `https://www.sciencedirect.com/science/article/pii/S0094576522002739`.

[34] E. Zimovan, K. Howell, and D. Davis. Near rectilinear halo orbits and their application in cis-lunar space. 05 2017.

List of Figures

2.1 Rotating and inertial frames 8
2.2 Representation of NRHO in various frames. 12
2.3 Zero velocity curves. 14
2.4 Zero velocity curves with equilibrium points. 16
2.5 Poincaré section pattern for a stable manifold. 17
2.6 Outer stable manifold 17
2.7 Fixed time differential corrector scheme 21
2.8 Variable time differential corrector scheme 22

3.1 Northern $EM - L_2$ halo families 26
3.2 Southern $EM - L_2$ halo families 27
3.3 Stability index as a function of the perilune radius for the L2 southern family of halos. 28
3.4 Jacobi constant and period as a function of the perilune radius for the L2 southern family of halos. 28
3.5 Northern $EM - L_2$ NRHO families 29
3.6 Southern $EM - L_2$ NRHO families 30
3.7 Sun placement in the rotating frame. 31
3.8 Eclipse geometry. 32
3.9 Eclipse behaviour due to primaries. 34
3.10 1 year eclipse behaviour. 35
3.11 Maximum eclipse orbits. 36
3.12 1 year total eclipse behaviour. 37

4.1 Manifolds for Halo in Earth-Moon system. 41
4.2 Required Δv to reach GTO from LEO. 42
4.3 Total Δv cost for different Halo parking orbit transfer. 46
4.4 Δv cost for the individual burns with GTO as parking orbit. 47
4.5 Total Δv cost for different Halo parking orbit transfer. 48
4.6 Δv cost for the individual burns with LEO as parking orbit. 49

4.7 Total Δv cost for different Halo parking orbit transfer. 50
4.8 Minimum Δv cost GTO. 51
4.9 Minimum Δv cost LEO. 51
4.10 Transfer to Halo with 40000 km perilune with GTO as park orbit. 54

5.1 Manifolds within the bounding sphere. 59
5.2 Process for optimal manifold pair selection. 61
5.3 Scheme of the optimizer problem. 62
5.4 Δv_{TOT} distribution with respect to Jacobi constant difference for Halo and NRHO options. 63
5.5 Δv_{UB} and Δv_{BS} distribution with respect to Jacobi constant difference between Halo and NRHO options. 63
5.6 Transfer between 40000 km and 6000 km perilune. 64

6.1 Mission scheme. 66
6.2 Multiple shooting scheme. 66
6.3 The first option: Transfer to an NRHO with 6000 km perilune and intermediate Halo with 40000 km perilune. 70
6.4 The second option: Transfer to an NRHO with 12000 km perilune and intermediate Halo with 36000 km perilune. 71
6.5 Distance to primaries during transfer for the first option. 72
6.6 Distance to primaries during transfer for the second option. 73

List of Tables

1.1 Missions related to Earth-Sun Lagrange points L_4, L_5 and L_2 3
1.2 Transfer options from Earth to EM L2 NRHO. 4

2.1 Non-dimesionalizing parameters for Earth-Moon system. 10
2.2 Lagrange points for Earth-Moon system. 16

3.1 Initial state for $EM - L_2$ Halo family generation. 25
3.2 Penumbra and umbra angles for primaries. 33

4.1 Refined results for the parking orbit to Halo transfer. 55

5.1 SOI parameters for Earth-Moon system 58

6.1 Transfer options from Earth to $EM - L_2$ NRHO. 68
6.2 Additional transfer options from Earth to $EM - L_2$ NRHO. 69

List of Symbols

Variable	Description	SI unit
$\boldsymbol{L}$	Lagrange point	-
$\boldsymbol{t}$	time	s
$\boldsymbol{m}$	mass	kg
$\boldsymbol{W}$	trajectory segment	-
$\boldsymbol{\mu}$	mass parameter	-
$\bar{\boldsymbol{r}}$	non-dimensional position vector	-
$\bar{\boldsymbol{R}}$	position vector	m
$\bar{\boldsymbol{v}}$	non-dimensional velocity vector	-
$\bar{\boldsymbol{V}}$	velocity vector	m/s
$\boldsymbol{U}$	pseudo-potential	-
$\boldsymbol{JC}$	Jacobi constant	-
$\boldsymbol{\tau}$	orbit period	-
$\boldsymbol{\beta}$	sun phase angle	-
$\boldsymbol{r_{SOI}}$	sphere of influence radius	m
$\boldsymbol{e}$	eccentricity	-
$\boldsymbol{h}$	angular momentum	m^2/s
$\boldsymbol{a}$	semi-major axis	m
$\boldsymbol{h_{norm}}$	normalized angular momentum	-
$\boldsymbol{\Phi}$	state transition matrix	-
$\boldsymbol{Y}$	eigenvector	-
$\boldsymbol{\lambda}$	eigenvalue	-
$\boldsymbol{V}$	normalized eigenvector	-
$\boldsymbol{\alpha}$	shadow angle	-

Acknowledgements

First of all, I would like to thank my family for their continuous support during my studies and the rough times of my life. Their care and energy provided me with the motivation and patience to finish this work. Also, I would to thank my advisor Professor Camilla Colombo and co-advisor Elisa Maria Alessi for their continuous guidance and support and their infinite patience. The advice and recommendations they provided on this thesis, helped me to enhance my understanding of the main topic deeply. Additionally, I am grateful to my teammate for the REMEC mission Marco Lo Iacono for his advice, corrections, and support.